Atmospheric Research 339 (2026) 109029

Contents lists available at ScienceDirect

Atmospheric Research

journal homepage: www.elsevier.com/locate/atmosres

WRF convective gray-zone simulations of the freshwater flux over the Ca Mau Peninsula, Southern Vietnam: Impacts of planetary boundary layer parameterizations

Duc Tran-Anh [a,b], Andreas H. Fink [b,*], Patrick Laux [a,d], Joël Arnault [a,d], Harald Kunstmann [a,d], Tan Phan-Van [c], Roderick van der Linden [b]

[a] IMK-IFU, Institute of Meteorology and Climate Research – Atmospheric Environmental Research, Karlsruhe Institute of Technology, Garmisch-Partenkirchen, Germany
[b] IMK-TRO, Institute of Meteorology and Climate Research – Troposphere Research, Karlsruhe Institute of Technology, Karlsruhe, Germany
[c] Faculty of Meteorology, Hydrology and Oceanography, VNU University of Science, Vietnam National University, Hanoi, Viet Nam
[d] Institute of Geography, University of Augsburg, Augsburg, Germany

ARTICLE INFO

Keywords:
Planetary boundary layer
Ca Mau Peninsula
Potential evapotranspiration
Diurnal cycle of precipitation
WRF model

ABSTRACT

Freshwater flux over the Ca Mau Peninsula, Southern Vietnam, is crucial for sustaining regional food production, ecosystem functioning, and the livelihoods of communities that rely on agriculture and aquaculture. This study examines the sensitivity of two components of the freshwater flux, namely, simulated precipitation and potential evapotranspiration (PET), to planetary boundary layer (PBL) schemes and diurnal sea surface temperature (SST) variability using the Weather Research and Forecasting (WRF) model over the Ca Mau Peninsula. Convective gray-zone (5 km) simulations were conducted for three representative years corresponding to El Niño, ENSO (El Niño – Southern Oscillation) neutral, and La Niña conditions, using ERA5 boundary conditions. Three PBL schemes (Mellor–Yamada–Nakanishi–Niino Level 2.5: MYNN2.5, Mellor–Yamada–Janjic: MYJ and Asymmetric Convection Model 2: ACM2) were tested with or without the activation of the SST skin temperature option. Simulated precipitation was evaluated against rain gauge observations and satellite-based datasets, while PET was assessed using station-based estimates derived from the Penman–Monteith method and ERA5 reanalysis data. The results indicate that MYNN2.5 and MYJ reproduce observed rainfall patterns more accurately than ACM2, which exhibits a pronounced wet bias. Incorporating diurnal SST variability reduces precipitation biases by 10–40%. All schemes capture the general features of the diurnal rainfall cycle, although nighttime rainfall is systematically underestimated; among them, MYNN2.5 most accurately represents both inland and coastal rainfall peaks. PET simulations are also sensitive to the choice of PBL scheme, with MYNN2.5 showing the lowest overall bias. Overall, the MYNN2.5 scheme combined with the diurnal SST option provides the most reliable representation of the freshwater flux over the Ca Mau Peninsula. These findings offer important insights for improving freshwater flux simulations over the Ca Mau Peninsula, the most important aquaculture hub in Vietnam.

1. Introduction

The freshwater flux, commonly expressed as the difference between precipitation and evapotranspiration, is a fundamental control on agricultural productivity, aquaculture sustainability, ecosystem functioning, and regional water supply in coastal and deltaic regions (Vörösmarty et al., 2000; Intergovernmental Panel on Climate Change (IPCC), 2014; Liu et al., 2018; Zhao et al., 2021; Mondal et al., 2022). The Ca Mau Peninsula, located in southern Vietnam and forming part of the Vietnamese Mekong Delta, represents the country's most important aquaculture hub and a major contributor to national rice production (Wilder and Phuong, 2002; Ha et al., 2013; General Statistics Office of Vietnam (GSO), 2019). The region experiences a tropical monsoon climate characterized by a highly asymmetric seasonal rainfall regime, where more than 90% of the annual precipitation occurs during the May–October rainy season, while rainfall during the January–March dry season is scarce (Lee and Dang, 2019). This strong seasonality results in a pronounced surplus of freshwater flux during the wet season and

* Corresponding author at: Institute of Meteorology and Climate Research – Troposphere Research, Karlsruhe Institute of Technology, Karlsruhe, Germany.
E-mail address: andreas.fink@kit.edu (A.H. Fink).

https://doi.org/10.1016/j.atmosres.2026.109029
Received 20 December 2025; Received in revised form 13 April 2026; Accepted 17 April 2026
Available online 18 April 2026

severe deficits during the dry season, posing substantial risks to irrigation, aquaculture operations, groundwater recharge, and domestic water supply (Minh et al., 2022a; Minh et al., 2022b; Kaveney et al., 2023). In addition, the freshwater flux in southern Vietnam is strongly modulated by large-scale climate variability, particularly ENSO (Duc et al., 2018; Luong, 2021). La Niña years are associated with earlier rainy-season onset, later rainy-season cessation, and higher rainfall totals, whereas El Niño years are characterized by shorter rainy seasons and reduced dry-season rainfall totals (Duc et al., 2018; Dang et al., 2020). Similarly, evapotranspiration is elevated during El Niño phases compared with La Niña phases, particularly during the October–May period (Luong, 2021).

Regional Climate Models (RCMs) offer one of the most effective tools for simulating the climate system in general, and freshwater flux in particular, at regional scales. Through their high spatial resolutions, RCMs are able to capture land–atmosphere interactions and represent regional forcings, such as large water bodies, surface vegetation, and complex topography, that exert significant influences on local climate (Giorgi, 1990; Gao et al., 2001). However, significant uncertainties and systematic biases persist in reproducing rainfall patterns over southern Vietnam (Phan et al., 2009; Nguyen et al., 2014; Raghavan et al., 2015), and particularly within the Vietnamese Mekong Delta (Jiang et al., 2019; Sun et al., 2021; Hoang-Cong et al., 2022; Fu et al., 2023; Trinh-Tuan et al., 2025). Previous RCM studies have predominantly employed horizontal resolutions ranging from 20 to 54 km, which are sufficient to resolve large-scale monsoon circulations but inadequate for mesoscale convective systems typical of the delta (Prein et al., 2015; Giorgi et al., 2016). Recent advancements in computational capacity have facilitated convection-permitting simulations at very high resolutions (~3 km or finer) in several regions (Hentgen et al., 2019; Kendon et al., 2021), enabling the explicit representation of convective processes. However, conducting such simulations remains computationally challenging, given the limitations of our current resources. Yet, high-resolution simulations are essential for producing more accurate assessments of the freshwater flux across the Mekong Delta. To balance computational efficiency and model performance, convective gray-zone resolutions (approximately 4–10 km, hereafter refer to gray-zone resolution for short) are widely employed for long-term regional climate simulations over Asia (Chen et al., 2018; Taraphdar and Pauluis, 2021; Hoang-Cong et al., 2022; Zhou et al., 2022). It is noteworthy that these resolutions are insufficient to explicitly resolve smaller convective systems but are yet too high to fully rely on convective parameterization (Taraphdar and Pauluis, 2021; Taraphdar et al., 2021). As highlighted by Taraphdar et al. (2021), gray-zone simulations can perform as well as convection-permitting simulations when appropriate physical parameterizations are employed to capture synoptic and mesoscale processes. Given that precipitation represents a primary component of the freshwater flux, alongside potential evapotranspiration (PET), accurate rainfall simulation at gray-zone resolution through the optimization of physical parameterizations is imperative for producing reliable assessments of the freshwater flux over the Mekong Delta.

PBL parameterizations play a pivotal role in regulating the exchange of momentum, heat, and moisture between the land surface, ocean, and atmosphere, thereby exerting a decisive influence on the simulation of low-level winds, cloud formation, and thermodynamic profiles (Garratt, 1994). Precipitation has been shown to exhibit pronounced sensitivity to the choice of PBL parameterization schemes, both at coarse resolutions (Laux et al., 2013; Wang et al., 2014; Que et al., 2016) and gray-zone resolution ranges (Taraphdar and Pauluis, 2021; Taraphdar et al., 2021) across the Asian summer monsoon domain. Beyond its seasonal variability, the diurnal cycle of precipitation during the rainy season constitutes a distinctive and influential feature of the Asian monsoon system, including Vietnam (Chen, 2020; Lai et al., 2025). The diurnal cycle is particularly important for the Ca Mau Peninsula, a major hub of agricultural and aquacultural activities, as shifts in the timing of rainfall peaks may have significant implications for agricultural processes, regional hydrological processes, and disaster risk management (Subrahmanyam et al., 2025). Previous studies have also confirmed that the representation of the diurnal precipitation cycle is highly sensitive to PBL parameterization schemes across Asia (Koo and Hong, 2010; Zhang and Chen, 2016; Yang et al., 2018; Mei et al., 2024).

In addition to PBL parameterization schemes, the diurnal variability of SST represents another critical process influencing rainfall simulations (Senatore et al., 2014; Pilatin et al., 2021). The Ca Mau Peninsula is located within the Tropical Warm Pool, a region globally recognized for its exceptionally high annual mean SST, weak surface winds, intense shortwave radiation under clear-sky conditions, and frequent large-amplitude diurnal SST fluctuations (Zhang et al., 2016). Previous investigations have demonstrated that explicitly accounting for diurnal SST variations improves the representation of air–sea coupling processes, thereby enhancing the performance of coupled climate models (Wei et al., 2001; Brunke et al., 2008; Clayson and Bogdanoff, 2015; Marullo et al., 2016). Since version 3.1, the WRF model, one of the most widely applied RCMs, has included a prognostic sea surface skin temperature (SSKT) scheme developed by Zeng and Beljaars (2005) through the sst_skin option. This scheme incorporates the effects of sensible and latent heat fluxes, radiative transfer, molecular diffusion, and turbulent mixing, thereby capturing the key mechanisms that drive diurnal SST variability. Evaluations over the Tropical Warm Pool have confirmed that the scheme successfully reproduces diurnal SST variations under a range of wind and radiation conditions (Zhang et al., 2018).

Unlike precipitation, PET, which constitutes the second major component of the freshwater flux, is not directly simulated by RCMs. Previous studies have attributed variations in PET primarily to sunshine duration or solar radiation (Li et al., 2015; Jiang et al., 2016; Xu et al., 2014), while other research highlights the dominant role of the wind speed at 10-m height (Li et al., 2014; Yin et al., 2010). Despite its importance, the sensitivity of PET to PBL parameterizations in RCMs remains insufficiently understood. Nonetheless, studies examining the influence of PBL schemes on two key drivers of PET, namely, the wind speed at 10-m height (Mohan and Bhati, 2011; Xie et al., 2012; Dzebre and Adaramola, 2020; Gholami et al., 2021) and solar radiation (Hu et al., 2010; Xie et al., 2012), provide strong evidence that PBL scheme selection exerts a significant effect on the simulation of PET.

Specifically, this study addresses the following research questions for the Ca Mau Peninsula study region: (1) how do different PBL parameterization schemes affect daily precipitation and the diurnal cycle of precipitation during the rainy season; (2) to what extent does the diurnal variability of SST, represented through the sst_skin option, influence daily precipitation and its diurnal cycle; and (3) how do different PBL parameterization schemes affect daily PET?

To answer these questions, we will conduct WRF simulations at 5-km gray-zone resolution for three representative years corresponding to El Niño, ENSO neutral, and La Niña conditions. The experiments systematically examine three widely used PBL schemes, both with and without activation of the sst_skin option. The remainder of this paper is organized as follows. Section 2 describes the model configuration, experimental design, and validation data. Section 3 presents the impacts of PBL parameterization schemes and SST diurnal variability on precipitation characteristics. Section 4 examines the corresponding sensitivity of PET. Section 5 summarizes the main findings and discusses their implications.

2. Data and methods

2.1. Data

Daily rainfall observations were collected from 25 meteorological stations distributed across the Ca Mau Peninsula (Fig. 1; Table S1). Three of these stations report to the World Meteorological Organization at 6-hourly intervals, and one reports real-time at the same frequency to the National Center for Hydro-Meteorological Forecasting of Vietnam.

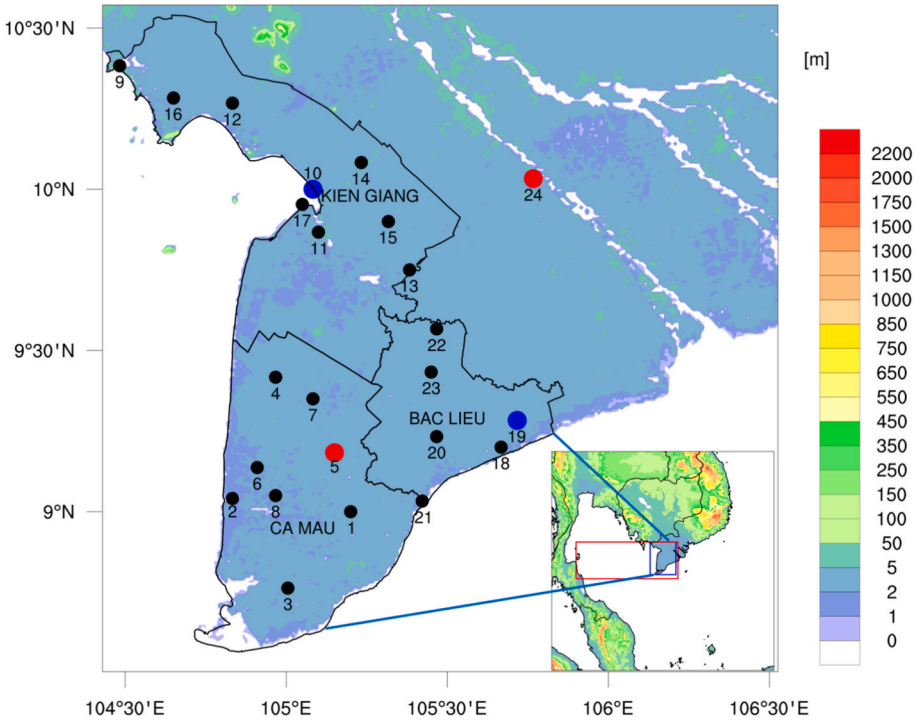

Fig. 1. Topography (shading), provinces in the Ca Mau Peninsula and model domain for WRF simulations (inset map). Text in capital letters indicates province names. In the inset map, the blue rectangle indicates the study region, while the red rectangle represents the area for analyzing the propagation of rainfall. Black points show rain gauge stations, blue points show stations from which sunshine duration data were used to calculate PET and red points show stations from which evaporation data were used (see Table S1 for station information). (For interpretation of the references to colour in this figure legend, the reader is referred to the web version of this article.)

Meteorological data, including maximum and minimum temperatures, relative humidity, sunshine duration, and 10-m wind speed from three stations covering the period 2007–2015, were used to compute PET using the Penman–Monteith method (Shuttleworth, 1993). For the validation of PET, evaporation data from the GGI-3000 evaporimeter were also employed. This instrument, formerly standard across the Soviet Union, measures daily open-water evaporation and is still maintained at two stations in the Mekong Delta (Ca Mau and Can Tho). Previous studies suggest that Penman–Monteith PET correlates reasonably with GGI-3000 observations, although it is typically biased high by

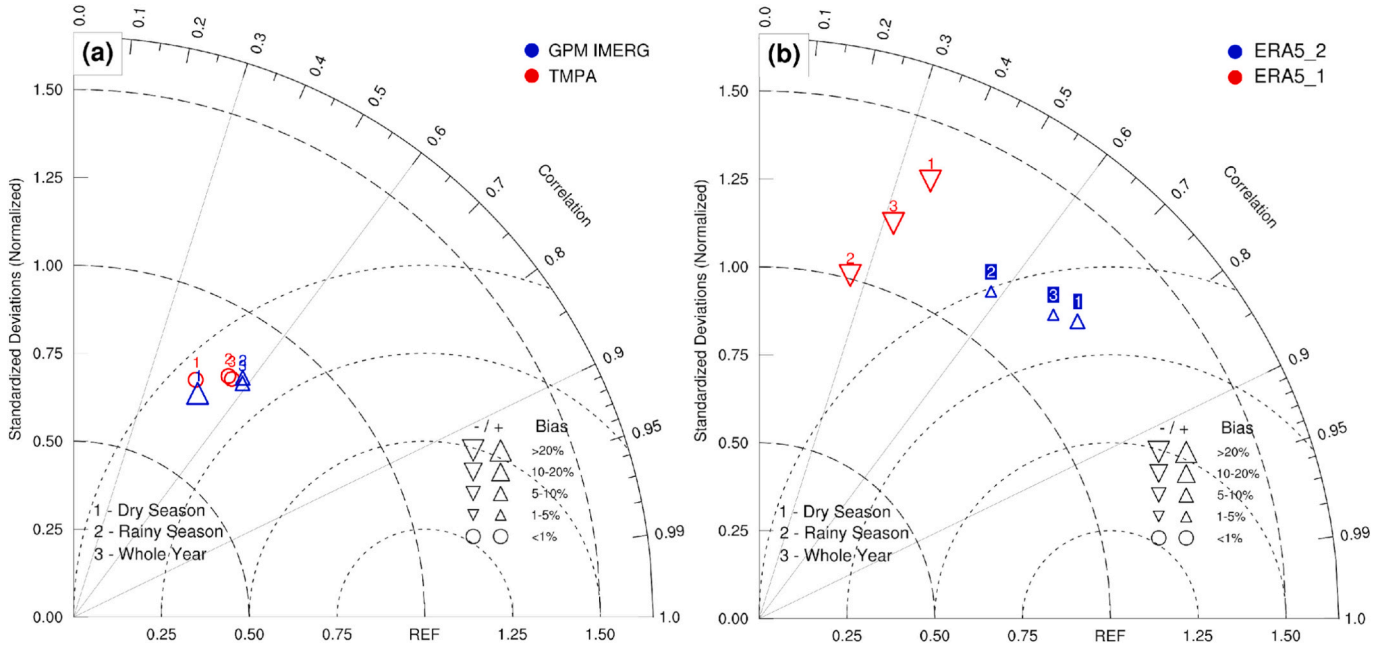

Fig. 2. Taylor diagrams of (a) daily TMPA (red symbols) and GPM IMERG rainfall (blue symbols) against observation at 24 stations, and (b) daily ERA5 PET evaluated against estimates using the Penman-Monteith equation (red symbols) and GGI-3000 measurements (blue symbols) for the rainy seasons, dry seasons, and whole years between 2007 and 2016. (For interpretation of the references to colour in this figure legend, the reader is referred to the web version of this article.)

~0.8 mm day^{-1} (Kohut et al., 2014; Stan and Neculau, 2015).

Moreover, rainfall validation was supported by two satellite-based products: the 3-hourly Tropical Rainfall Measuring Mission (TRMM) 3B42 V7 (TMPA) dataset at a 0.25° × 0.25° resolution (Huffman and Bolvin, 2014) and the daily CHIRPS 2.0 dataset at a 0.05° × 0.05° resolution (Funk et al., 2015). TMPA generally performs better for rainfall estimation in the Mekong Delta, whereas CHIRPS provides higher spatial detail and drought monitoring capability (Guo et al., 2017; Luo et al., 2019; Dinh et al., 2020). For the Ca Mau Peninsula, TMPA outperformed its successor, the latest GPM IMERG Version 06 (Hou et al., 2014), which has a spatial resolution of 0.1° × 0.1°, when compared against gauge data using Taylor diagram analysis (Taylor, 2001; Fig. 2a). As shown in Fig. 2a, the GPM product exhibits a systematic overestimation of rainfall, with positive PBIAS values of approximately 5–10% during the rainy season and 10–20% during the dry season. In contrast, the TMPA product demonstrates markedly better agreement with observations, with absolute PBIAS values consistently below 1% in both seasons. Additionally, to examine the diurnal cycle, 3-hourly rainfall from 14 automatic stations during 2019–2020 was also used to validate TMPA estimation. These results indicate that TMPA performs well in terms of estimating precipitation amount, precipitation frequency, and precipitation intensity (not shown).

Given the limited distribution of ground-based PET measurements, validation against gridded datasets was also undertaken. Several global PET products are available, including satellite-based datasets such as GLEAM (Martens et al., 2017), MODIS MOD16 (Mu et al., 2011), TerraClimate (Abatzoglou et al., 2018), as well as reanalysis datasets such as ERA5 (Hersbach et al., 2020), JRA-55 (Kobayashi et al., 2015), and MERRA-2 (Gelaro et al., 2017). Among these, ERA5 PET was selected and evaluated for 2007–2016 against Penman–Monteith estimates at Ca

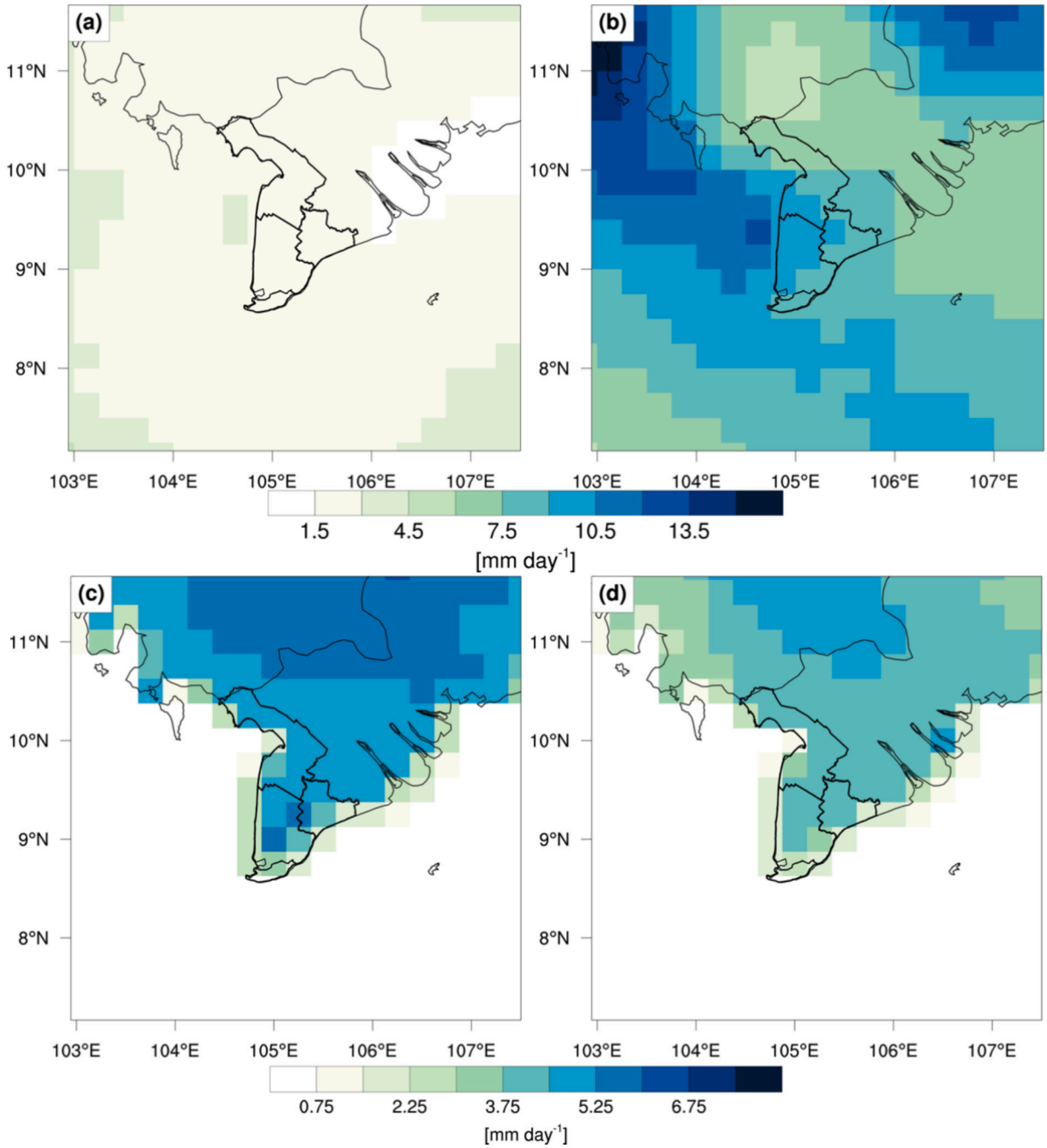

Fig. 3. Mean daily TMPA rainfall (a) in the dry seasons and (b) in the rainy seasons in the period 2008–2017. (c, d) Same as in (a, b) but for mean daily ERA5 PET.

Mau, Rach Gia, and Bac Lieu, and against GGI-3000 data at Ca Mau and Bac Lieu (Fig. 2b). ERA5 PET showed stronger agreement in the dry season (correlation of 0.75 against GGI-3000) than in the rainy season (0.59), while correlations against Penman–Monteith were lower (0.35 and 0.25). ERA5 PET is computed under the assumption of well-watered land surfaces (i.e., without soil moisture stress), with vegetation parameters prescribed as "crops/mixed farming" (Hersbach et al., 2023). These assumptions differ from local land-surface conditions and from the inputs used in station-based Penman–Monteith calculations and the GGI-3000 dataset, which limits direct comparability. Overall, the evaluation results indicate that ERA5 provides a physically consistent and temporally coherent reference for validating simulated PET. The mean daily TMPA rainfall and ERA5 PET during the dry and rainy seasons over the Ca Mau Peninsula for 2008–2017 are presented in Fig. 3.

2.2. Methods

2.2.1. Model description and experimental design

The Advanced Research WRF model version 4.0 (Skamarock et al., 2019) is applied to simulate precipitation and PET over the Ca Mau Peninsula. The model domain covers the Ca Mau Peninsula and adjacent regions, including Central Vietnam, Cambodia, Southern Laos, and Northeastern Thailand (98.4–112°E, 2.6–16°N; Fig. 1). The domain resolution is set at 5 km, with 300 × 300 horizontal grid points, 37 vertical levels, and the model top at 10 hPa. Boundary and initial conditions are provided by the ERA5 reanalysis (Hersbach et al., 2020) at a resolution of ~30 km and a temporal frequency of 3 h. To assess climate variability, three representative years are selected based on the Niño 3.4 index from the NOAA Climate Prediction Center (Climate Prediction Center (CPC), NOAA, 2025): 2007 (La Niña), 2013 (ENSO-neutral), and 2015 (strong El Niño). Simulations are initialized on 1 December of the preceding year and include a 30-day spin-up to allow the model to be geared toward "climate mode" after 30 days of spin-up time (Zhong et al., 2007).

A suite of sensitivity experiments is designed to evaluate the role of key physical parameterizations. Three widely used PBL parameterization schemes were selected: MYNN2.5 (Mellor–Yamada–Nakanishi–Niino Level 2.5, Nakanishi and Niino, 2006), Mellor–Yamada–Janjic (MYJ; Janjić, 1994), and Asymmetric Convection Model 2 (ACM2; Pleim, 2007). These schemes represent contrasting treatments of turbulent transport and have been extensively applied in regional climate simulations over monsoon-dominated regions (Wang et al., 2014; Que et al., 2016; Jia et al., 2023; Shen and Du, 2023).

MYNN2.5 and MYJ are local turbulent kinetic energy (TKE)-based closure schemes in which vertical mixing is determined by prognostic TKE and local stability-dependent diffusion coefficients. In contrast, ACM2 employs a hybrid formulation that combines local eddy diffusion with an explicit nonlocal transport component to represent organized large eddies within the convective boundary layer. Although WRF model includes additional nonlocal-type PBL schemes, ACM2 was chosen here as a representative hybrid framework to contrast local TKE-based closures with a scheme that incorporates both local and nonlocal mixing characteristics. These structural differences can lead to systematic variations in vertical turbulent diffusion coefficients, entrainment at the PBL top, boundary-layer depth, and surface flux partitioning (Pleim, 2007). In tropical coastal environments such as the Ca Mau Peninsula, where land–sea thermal contrasts and strong surface fluxes regulate low-level moisture supply and convective development, the representation of vertical mixing is expected to exert a significant influence on moisture convergence, precipitation timing and intensity, and near-surface wind fields that affect PET. The selected schemes therefore provide a suitable framework for examining how differences in turbulent transport assumptions propagate into variations in simulated freshwater flux components.

Each scheme is paired with its corresponding surface-layer scheme and further tested with or without the activation of the sst_skin option of Zeng and Beljaars (2005), resulting in six baseline experiments (Table 1). The sst_skin option accounts for sensible and latent heat fluxes, radiative forcing, and turbulent diffusion, and has been shown to improve representation of diurnal SST variability in tropical oceans. To address limitations at gray-zone resolutions, additional experiments are conducted for the year 2015, a strong El Niño year, with MYNN2.5 PBL scheme coupled to five cumulus schemes: Kain–Fritsch (Kain 2004), Betts–Miller–Janjic (Janjic 1994), Grell–Freitas (Grell and Freitas, 2014), New Simplified Arakawa–Schubert (Kwon and Hong, 2017), and Grell 3D Ensemble (Grell and Devenyi, 2002) to examine the influence of cumulus scheme on simulating precipitation (Table S2). Our results show that the convection-permitting simulation experiment (WRF-MYNN2.5, which does not utilize any of the cumulus schemes) outperforms other cumulus scheme experiments over the Ca Mau Peninsula and will be used in later experiments (Table S4 and Fig. S1).

Physics parameterizations unrelated to the PBL are selected following common WRF practices in Southeast Asia: WSM6 microphysics (Hong and Lim, 2006), Dudhia shortwave radiation (Dudhia, 1989), RRTM longwave radiation (Mlawer et al., 1997), and the Noah-MP land surface scheme (Yang et al., 2011; Niu et al., 2011). Together, these simulations allow for a comprehensive assessment of the sensitivity of precipitation and PET to the PBL scheme and the sst_skin option under contrasting ENSO conditions.

2.2.2. PET estimation

The presented analyses rely on the evaluation of PET using both observation data from stations and model simulations using the WRF model. In both cases, the Penman-Monteith equation (Shuttleworth, 1993) is used for calculating PET:

$$PET = \frac{\Delta}{\Delta+\gamma}(R_n + A_h) + \frac{\gamma}{\Delta+\gamma}\frac{6.43(1+0.536U_2)D}{\lambda} \quad (1)$$

Where PET is the daily PET in mm day^{-1}, R_n is the surface net radiation in MJ m^{-2} day^{-1}, A_h is the energy advected to the water body, which is ignored in this study, U_2 is the near-surface wind speed at 2-m height in m s^{-1}, Δ is the slope of air pressure curve in kPa °C^{-1}, D is the vapor pressure deficit in kPa, γ is the psychrometric coefficient in kPa °C^{-1} and λ is the latent heat of water vaporization in MJ kg^{-1}. Since U_2 is not directly available, it is determined from wind speed at 10-m height as follows:

$$U_2 = \frac{4.87}{ln(67.8*10-5.42)}\,U_{10} \quad (2)$$

Where U_{10} is the surface wind speed at 10-m height in m s^{-1}.

The approach to determine R_n differs between station and model data. For station data, R_n is determined as:

$$R_n = 0.77R_s - 0.5\sigma\left(T_{max}^4 + T_{min}^4\right)(0.34 - 0.14\sqrt{e_a})\left(1.35\frac{R_s}{R_{s0}} - 0.35\right) \quad (3)$$

$$R_s = R_a\left(a + b\frac{n}{N}\right) \quad (4)$$

Table 1
Details of WRF Configurations for: different PBL scheme, corresponding surface layer scheme, sst_skin option (on/off). No cumulus parameterization is used in these baseline simulations at 5-km gray-zone resolution.

Experiment Name	PBL scheme	Surface Layer scheme	sst_skin option
WRF-MYNN2.5	MYNN2.5	MYNN	On
WRF-MYJ	MYJ	ETA	On
WRF-ACM2	ACM2	MM5	On
WRF-MYNN2.5-s	MYNN2.5	MYNN	Off
WRF-MYJ-s	MYJ	ETA	Off
WRF-ACM2-s	ACM2	MM5	Off

$$R_{s0} = R_s\left(0.75 + 2{*}10^{-5}{*}z\right) \quad (5)$$

Where R_s is the solar radiation in MJ m^{-2} day^{-1}, σ is the Stefan-Boltzmann constant for a day (4.903×10^{-9} MJ K^{-4} m^{-2} day^{-1}), T_{max} and T_{min} are the maximum and minimum temperature at 2 m height in Kelvin, e_a is the actual vapor pressure in kPa, R_{s0} is the clear-sky solar radiation in MJ m^{-2} day^{-1}, R_a is the extraterrestrial radiation in MJ m^{-2} day^{-1}, a and b are empirical coefficients (a = 0.25 and b = 0.5), n is the actual sunshine duration in hour, N is the maximum possible sunshine duration in hour, and z is the station elevation above the sea in m.

For WRF simulations, R_n is determined through the accumulated net radiative flux at the surface field from 1200 UTC on the previous day to 1200 UTC on the current day:

$$R_n = \sum_{t=-12}^{t=12} R_{swu} + R_{swd} + R_{lwu} + R_{lwd} \quad (6)$$

Where R_{swu} is the upward shortwave radiation, R_{swd} the downward shortwave, R_{lwu} the upward longwave radiation, and R_{lwd} the downward longwave radiation (at the surface and in MJ m^{-2}).

As previously reported (Donohue et al., 2010; Dai, 2011), the Penman-Monteith formula has demonstrated better performance than other formulas in estimating PET.

2.2.3. Evaluation methods

To statistically compare the performance of each WRF experiment against the gridded products, PET and precipitation fields from WRF model output were first remapped to 0.25° spatial resolution to match the TMPA and ERA5 grids, and to 0.05° spatial resolution to match the CHIRPS 2.0 grid using conservative remapping (Jones, 1999). After remapping, these data are evaluated based on three basic statistical indices, the correlation coefficient (CC), RMSE and percent bias (PBIAS), which are defined as:

$$CC = \frac{\sum_{i=1}^{n}(O_i - \underline{O})(P_i - \underline{P})}{\sqrt{\sum_{i=1}^{n}(O_i - \underline{O})^2}\sqrt{\sum_{i=1}^{n}(P_i - \underline{P})^2}} \quad (7)$$

$$RMSE = \sqrt{\frac{1}{n}\sum_{i=1}^{n}(O_i - P_i)^2} \quad (8)$$

$$PBIAS = \frac{\sum_{i=1}^{n}(P_i - O_i)}{\sum_{i=1}^{n} O_i} \times 100 \quad (9)$$

Where n is the number of samples, O_i is the observed precipitation or PET, and P_i is the simulated precipitation or PET from WRF output.

Regarding the statistical evaluation against station data, the simulated precipitation or PET are interpolated using values from the closest four grid points to the station locations. Instead of evaluating by three separate indices, all indices are represented in a Taylor diagram (Taylor, 2001), which combines these three values into a single point. The Taylor diagram evaluations for the WRF experiments using different PBL schemes are provided in Fig. 7(a) for daily precipitation and in Fig. 13 for PET. To simplify evaluations for different variables with different units, the RMSE and standard deviation are normalized by the observed standard deviation of each variable before plotting (Taylor, 2001). CC values imply the temporal and spatial similarity between the observation at the station and the simulated precipitation or PET from the WRF output. In the diagram, the azimuthal angle corresponds to the CC, the dashed line (labelled "REF") shows the normalized standard deviation of the observation, and the dotted semicircles, originating from the intersection of the observed standard deviation (dashed line) and the horizontal axis, show contours of the normalized RMSE. Experiments with the smallest RMSE are highlighted with a colour-filled background of the number indicating the station location. Locations with negative correlations or standard deviations greater than 1.65 are shown as text at the bottom of each Taylor diagram.

In southern Vietnam, precipitation exhibits strong seasonality (Phan et al., 2009; Truong and Bui, 2019; Truong and Tuan, 2018). For this reason, the evaluation of the performance of each WRF experiment on simulating daily precipitation is conducted in terms of the dry season, the rainy season, and the whole year. In adition, intraseasonal oscillation (ISO) plays a vital role in modulating rainfall in Vietnam, with two dominant modes of oscillation: 10–20 and 20–60 days (Truong and Bui, 2019; Truong and Tuan, 2018). Consequently, the performance of each experiment on simulating 5 and 10 days of accumulated precipitation is also evaluated.

Following previous studies (Takahashi et al., 2010; Jin et al., 2016; Li et al., 2020), to describe the characteristics of the diurnal cycle of precipitation over the Ca Mau Peninsula, three parameters are calculated from both model data and TMPA product at each 3-h time step, including rainfall frequency, rainfall amount, and rainfall intensity. The rainfall frequency is defined as the percentage of time that a measurable amount of rainfall falls during the analysis period, while rainfall intensity is the mean precipitation rate during the precipitating time. The rainfall amount is the product of rainfall intensity and rainfall frequency. The threshold for measurable rainfall rate used in this study is 0.2 mm h^{-1}.

3. Results and discussion

3.1. Role of the sst_skin option on simulated daily precipitation

The section discusses the impact of the sst_skin option on simulated daily precipitation. The difference in PBIAS, |PBIAS|, and RMSE against TMPA between daily precipitation for simulation WRF-MYNN2.5-s (not activated the sst_skin option) and simulation WRF-MYNN2.5 (activated the sst_skin option) is shown in Fig. 4. During the rainy season, activating the sst_skin option systematically reduces the dry bias of WRF-MYNN2.5 over both land and adjacent ocean areas. Over the Ca Mau Peninsula, the precipitation bias decreases from approximately −40% to about −10%, corresponding to a reduction in absolute bias magnitude of nearly 30%. Similar reductions of 10–40% are evident over the surrounding ocean, indicating that the improvement is not confined to land but extends offshore.

The spatial distribution of |PBIAS| confirms that these changes represent genuine reductions in bias magnitude rather than a simple shift in bias sign. Most coastal and offshore grid points show positive |PBIAS| differences of 10–40%, demonstrating that rainfall underestimation is substantially alleviated when the sst_skin option is activated. In contrast, differences in RMSE remain relatively small, generally below 2 mm day^{-1} in both seasons, indicating that the primary improvement lies in the reduction of systematic bias rather than random error.

Physically, these improvements can be attributed to the more realistic representation of diurnal SST variability. In WRF, the sst_skin option computes a prognostic sea-surface skin temperature following the formulation of Zeng and Beljaars (2005), allowing SST to respond dynamically to radiative forcing and turbulent fluxes. By modifying the diurnal evolution of SST, the scheme alters surface sensible and latent heat fluxes, thereby influencing low-level thermodynamic instability and moisture availability. In tropical coastal environments such as the Ca Mau Peninsula, where the land–sea thermal contrast strongly modulates sea-breeze circulations, enhanced daytime SST warming can intensify onshore flow and low-level convergence. This convergence is a well-recognized trigger for moist convection and supports inland propagation of precipitation systems, particularly during periods when large-scale synoptic forcing is weak (Zhu et al., 2017).

The stronger coupling between SST variability and surface turbulent fluxes, therefore, helps mitigate the systematic rainfall underestimation in the simulations activated the sst_skin option. The fact that bias reductions of up to 40% occur over both land and adjacent ocean regions underscores the importance of accurately representing air–sea interaction processes in tropical peninsular settings. These results demonstrate that improvements in precipitation simulation are dynamically

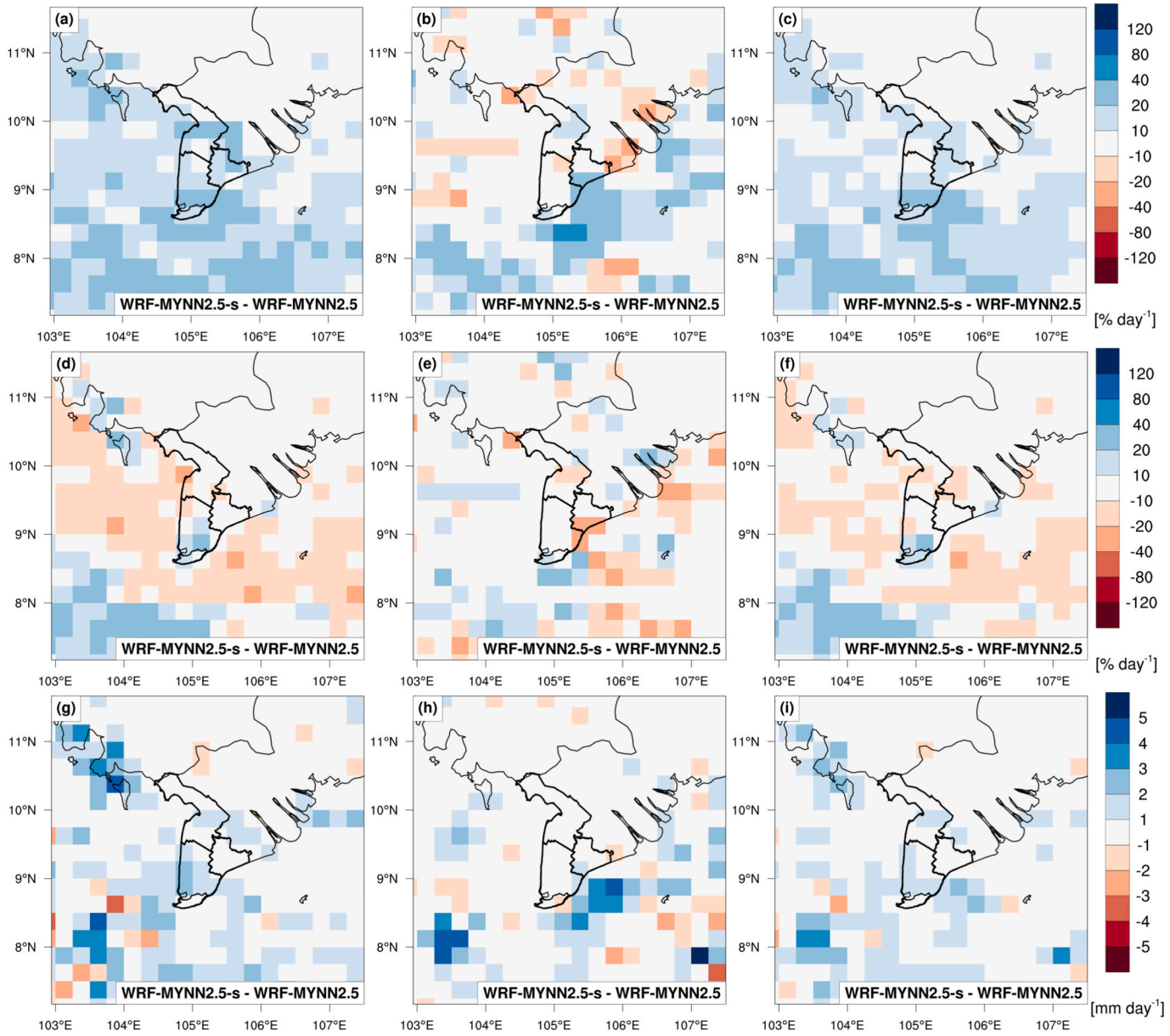

Fig. 4. The difference in PBIAS against TMPA between simulated daily rainfall of WRF-MYNN2.5-s and WRF-MYNN2.5 in (a) rainy seasons, (b) dry seasons, and (c) whole years in 2007, 2013, and 2015. (d-f) Same as in (a-c) but for |PBIAS| against TMPA. (g-h) Same as in (a-c) but for RMSE against TMPA.

consistent with enhanced surface heat and moisture exchange and their influence on mesoscale coastal circulations.

3.2. Role of the PBL parameterization schemes on simulated daily precipitation

The section illustrates the impact of the PBL parameterization scheme on simulated daily precipitation over the Ca Mau Peninsula. Figs. 5 and 6 present the PBIAS and RMSE of daily precipitation for simulation WRF-MYNN2.5, WRF-MYJ, and WRF-ACM2 for the period 2007–2013-2015 against TMPA. Particularly, our WRF-ACM2 experiments with the non-local PBL parameterization scheme ACM2 produce much more precipitation over the Ca Mau Peninsula and the surrounding ocean in both the dry and rainy seasons, with PBIAS ranging from 10 to 40% over the ocean region and 40 to 80% over the Ca Mau Peninsula. This is in good agreement with previous results by Wang et al. (2014), and these deviations correspond with the stronger low-level southwesterly flow over the East Asian summer monsoon.

For the two experiments employing local PBL parameterization schemes (WRF-MYJ and WRF-MYNN2.5), contrasting PBIAS in simulated rainfall is evident over the Ca Mau Peninsula. WRF-MYNN2.5 systematically underestimates precipitation in both the dry and rainy seasons, with negative PBIAS values ranging from approximately −10% to −20%. In contrast, WRF-MYJ exhibits a pronounced seasonal dependence, with daily rainfall being substantially overestimated during the dry season, resulting in PBIAS values ranging from 20% to 80%. Conversely, an underestimation is observed during the rainy season, with PBIAS ranging from −20% to 10%. As shown in Fig. 6, the differences in RMSE against TMPA between WRF-MYJ and WRF-MYNN2.5 are minor in both seasons. RMSE values for both experiments range from approximately 16–20 mm day^{-1} during the rainy season and 4–8 mm mm day^{-1} during the dry season. By contrast, WRF-ACM2 underperforms, exhibiting larger errors with RMSE values of about 20–24 mm mm day^{-1} in the rainy season and 8–12 mm day^{-1} in the dry season.

Figs. S2 and S3 report the PBIAS and RMSE of daily precipitation for the WRF-MYNN2.5, WRF-MYJ, and WRF-ACM2 simulations for the

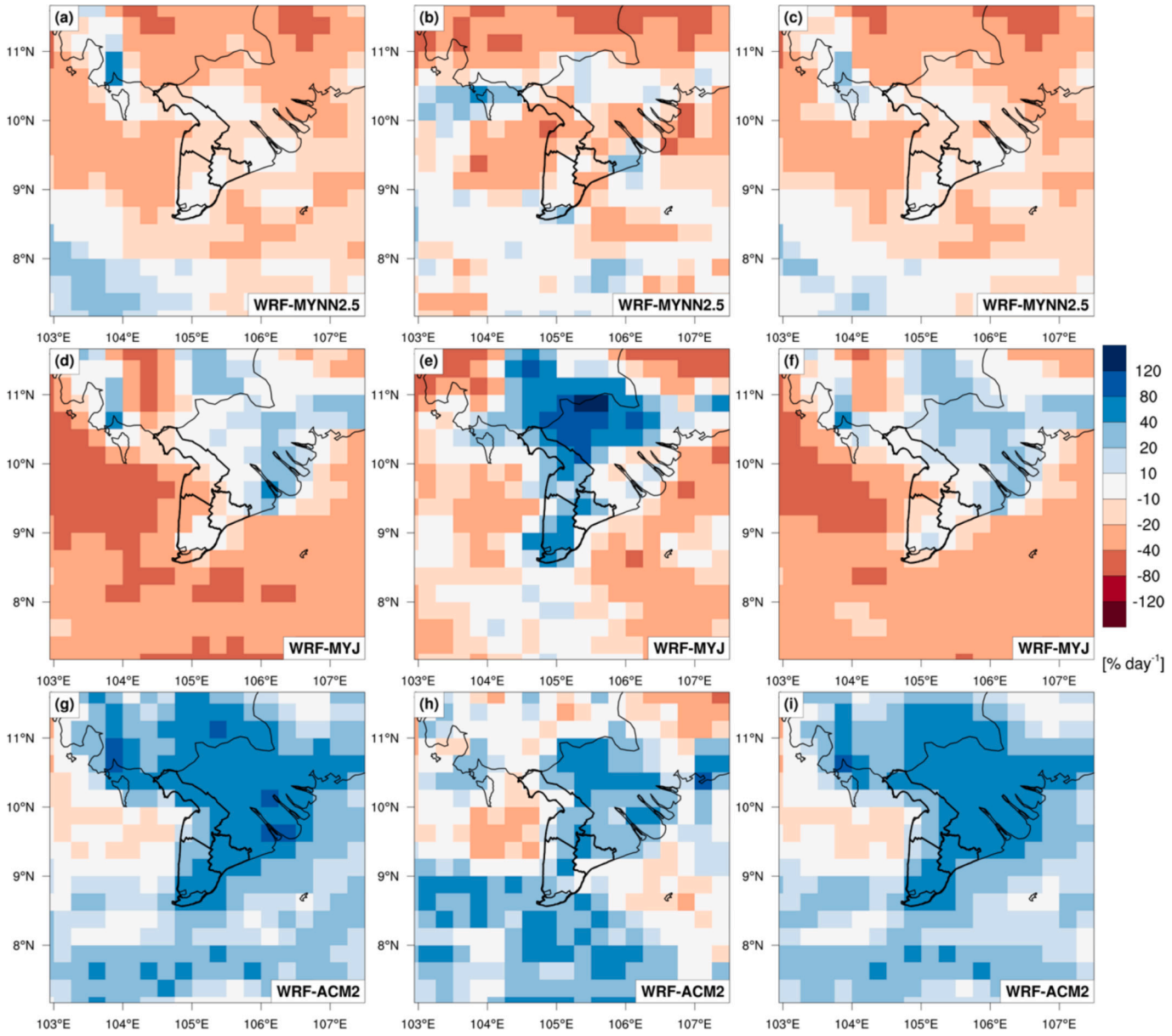

Fig. 5. The performance of WRF experiments using different PBL parameterization schemes is illustrated by the PBIAS of daily rainfall relative to TMPA for the rainy (first column), dry (second column), and annual (third column) periods, in average for the years 2007, 2013, and 2015. Panels (a–c), (d–f), and (g–i) correspond to results from the WRF-MYNN2.5, WRF-MYJ, and WRF-ACM2 experiments, respectively.

period 2007–2013-2015 against CHIRPS 2.0. The superiority of CHIRPS 2.0 lies in its high spatial resolution of 0.05°, which is expected to capture more representative precipitation characteristics (Duan et al., 2016). Furthermore, Guo et al. (2017) demonstrated that CHIRPS 2.0 shows reasonable ability to identify and characterize drought events; thus, CHIRPS 2.0 is a reliable dataset, especially in the dry season. It is important to note that the daily rainfall, in this case, was accumulated over 24 h starting at 0000 UTC (0700 LT). There were no significant differences between PBIAS and RMSE of each WRF experiment against TMPA and CHIRPS 2.0 products, despite the fact that the CHIRPS 2.0 resolution is finer than that of TMPA. The simulated rainfall amount from WRF-ACM2 shows inferior performance in both the dry and rainy seasons, with the highest RMSE and positive PBIAS values over the Ca Mau Peninsula. WRF-MYNN2.5 underestimates rainfall in both the rainy and dry seasons, while WRF-MYJ underestimates rainfall in the rainy season but overestimates in the dry season.

To quantitatively assess the performance of each WRF experiment, the PBIAS and RMSE of simulated daily rainfall compared to measurements at 24 stations, CHIRPS v2.0, and TMPA products over the Ca Mau Peninsula are listed in Table 2. For the dry season, the WRF-MYNN2.5 experiment provided the smallest RMSE; conversely, the WRF-MYJ experiment reproduced the smallest RMSE in the rainy season Regarding the entire year, the WRF-MYJ experiment showed the smallest RMSE; however, the differences between the RMSE of the WRF-MYJ and WRF-MYNN2.5 experiments are negligible. In general, WRF-MYJ and WRF-MYNN2.5 experiments have comparable performance in simulating daily precipitation; apart from them, the WRF-ACM2 experiment has the worst performance.

Fig. 7 presents the Taylor diagrams of daily, 5-day accumulated precipitation, and 10-day accumulated precipitation over 25 stations in the Ca Mau Peninsula in the dry season, rainy season, and the whole year for the period 2007–2013-2015. As shown in this figure, the CC value of daily precipitation in both dry and rainy seasons from three WRF experiments is relatively weak, about 0.30; the normalized standard

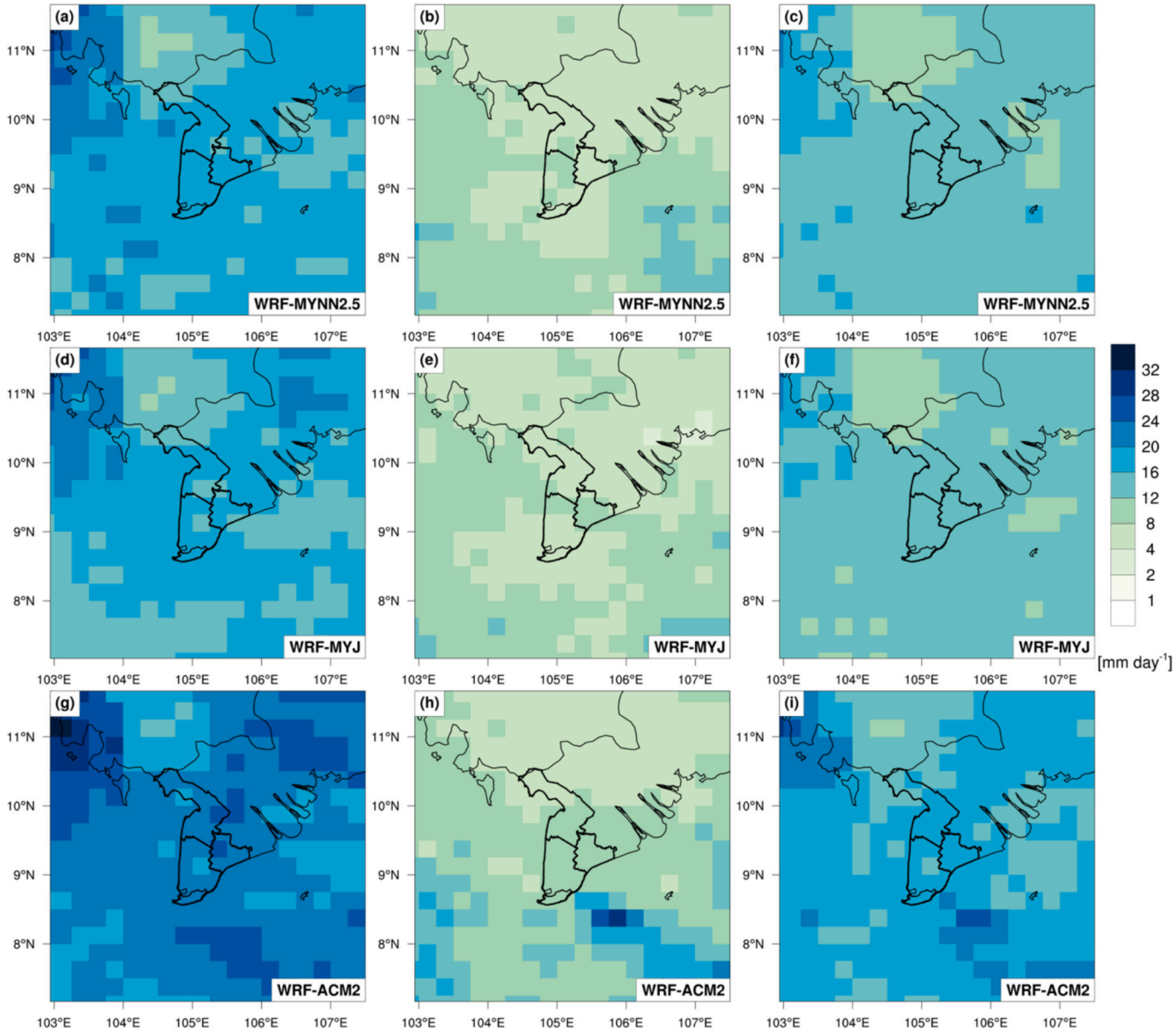

Fig. 6. Same as in Fig. 5 but for RMSE of simulated daily rainfall.

deviation of WRF-ACM2 is always highest, ranging from 1.1 to 1.4. Based on the colour-filled background, which indicates the experiment with the lowest RMSE, the experiment with the MYJ scheme overwhelms the simulation of daily precipitation in the rainy season and in the whole year. With respect to 5 days accumulated precipitation, the CC values from three experiments substantially increase, about 0.4–0.6, the standard deviation of WRF-ACM2 still has the highest values, between 1.1 and 1.4, and experiment WRF-MYNN2.5 performs better than the other two experiments in the dry season and in the whole year. In terms of 10 days accumulated precipitation, the CC values from the three experiments range from 0.4 to 0.65; experiment MYJ outperforms in the rainy season and in the whole year. Taken together, these results suggest that WRF-MYNN2.5 has better skills compared to the others in the dry season, while WRF-MYJ outperforms in the rainy season.

For a detailed view of the performance of each experiment in simulating daily precipitation over the Ca Mau Peninsula, Fig. S5 presents the Taylor diagram of daily precipitation for the separate years 2007, 2013, and 2015. Taken as a whole, all experiments have the best performance in 2015 (the year with strong El Niño conditions) with the highest CC, a range of 0.33 to 0.40, and the smallest normalized RMSE. In all three years, WRF-ACM2 has the worst performance with the highest normalized standard deviation ranging from 1.29 to 1.35, and the lowest CC between 0.28 and 0.33. It is worth noting that in 2015 (a year with strong El Niño conditions) and 2007 (a year with strong La Niña conditions), WRF-MYNN2.5 performed well compared to the other experiments, while in 2013 (a year with neutral conditions), WRF-MYJ had the best skill in simulating daily precipitation.

3.3. Role of the PBL parameterization schemes and sst_skin option on simulated diurnal cycle of precipitation during rainy seasons

In the current section, we next evaluate the diurnal cycle of precipitation simulated by all WRF experiments against the TMPA dataset, to explore the role of the PBL schemes and the sst_skin option on the simulated diurnal cycle of precipitation during rainy seasons over the Ca Mau Peninsula. For clarity, all analyses are presented in local time (LT; UTC + 7), which facilitates a direct comparison of daytime and nighttime precipitation characteristics. Model-simulated rainfall was

Table 2
PBIAS and RMSE of simulated daily rainfall compared to measurements at 24 stations, and CHIRPS 2.0 and TMPA satellite-based rainfall estimates over the Ca Mau Peninsula in 2007, 2013 and 2015. Bold numbers indicate experiments with lowest values of RMSE for each time period.

Experiment Name	WRF-MYNN2.5	WRF-MYJ	WRF-ACM2	WRF-MYNN2.5	WRF-MYJ	WRF-ACM2
	PBIAS (%)			RMSE (mm)		
Stations						
Rainy season	−16.14	−16.42	35.22	20.25	19.84	26.42
Dry season	−22.24	20.33	9.35	9.70	10.45	11.37
Year	−17.02	−17.02	30.73	15.89	15.87	20.36
TMPA						
Rainy season	−7.02	−10.00	47.72	16.92	16.34	24.30
Dry season	−29.20	11.70	0.70	7.49	8.63	9.66
Year	−11.32	−5.77	38.57	13.12	13.10	18.55
CHIRPS						
Rainy season	−8.12	−12.72	44.59	17.37	17.13	22.55
Dry season	−6.13	37.54	28.49	7.47	7.82	8.97
Year	−4.91	−3.85	43.79	13.37	13.35	17.23

composited into 3-hly intervals beginning at 0000 LT, consistent with TMPA.

Firstly, the role of PBL parameterization schemes in simulating the diurnal cycle of precipitation during rainy seasons is investigated. Fig. 8 displays the diurnal variations in rainfall frequency and rainfall amount averaged over the Ca Mau Peninsula during the rainy seasons of 2007, 2013, and 2015 from the WRF experiment with different PBL parameterization schemes and the sst_skin option activated. According to TMPA, rainfall frequency and intensity exhibit a pronounced afternoon maximum between 1300 and 1600 LT, in agreement with the findings of Takahashi et al. (2010), who identified an early-afternoon peak over coastal Indochina. The WRF simulations can reasonably mimic the 24-h evolution of rainfall, in terms of frequency and amount, although the rainfall frequency is generally underestimated. They can also capture the timing of the early afternoon peak of rainfall frequency and rainfall intensity, and the suppressed rainfall amount at night (2200–0100 LT), but fail to reproduce the suppressed rainfall frequency in the early morning (0400–0700 LT). Overall, all conducted gray-zone experiments show good performance in reproducing the diurnal cycle of precipitation. These results are consistent with recent findings by Lai et al. (2025), who demonstrated that high-resolution WRF simulations more accurately capture the diurnal cycle of summer rainfall over Mainland Southeast Asia, particularly along coastal and mountainous zones, than coarser reanalysis products.

It is found that the difference in the magnitude of diurnal rainfall between all experiments and TMPA is mainly attributed to the difference in nighttime (1900–0700 LT). No appreciable differences are found in simulated rainfall frequency among the three experiments. Conversely, simulated rainfall intensity from WRF-ACM2 is highly overestimated compared to TMPA and other experiments. Similar to the performance in simulating the seasonal variation of daily precipitation, the two experiments, WRF-MYNN2.5 and WRF-MYJ, can reproduce the diurnal cycle of rainfall more closely to the observed values over the Ca Mau Peninsula. Fig. 9 details the 3-hour mean in 1300–1600 LT (peak of the diurnal cycle) of rainfall intensity for the rainy season from TMPA observation, and the difference with three experiments. The results reveal that, compared to other experiments, WRF-MYNN2.5 appears to reproduce a more reasonable rainfall intensity with the smallest bias, especially over the western coastline of the Ca Mau Peninsula. This result points to the probability that WRF-MYNN2.5 is able to more accurately reproduce the convective systems that develop over the surrounding seas of the Ca Mau Peninsula and propagate to the western coastline.

To illustrate the tendency of diurnal rainfall cycle migration over the Ca Mau Peninsula during the rainy season, we use a Hovmöller diagram to capture the propagation along with its temporal evolution. The red box in Fig. 1, whose long sides are roughly perpendicular to the western coastline of the Ca Mau Peninsula, was defined to analyze this propagation. Fig. 10 shows the Hovmöller diagram for the time-coastal distance cross-sections averaged along the coastal direction, based on TMPA as well as all WRF simulations for the aforementioned box.

According to TMPA, it is possible to confirm that there is an early morning peak over the eastern Gulf of Thailand, approximately 200 km away from the western coastline of the Ca Mau Peninsula. This peak then migrates eastward along the coastline, into the inland area, and results in a maximum by early afternoon. This early morning peak fits with the previous finding of Takahashi et al. (2010), who identified three early morning peaks over the Indochina peninsula area, including the eastern Bay of Bengal, the eastern Khorat Plateau, and the eastern Gulf of Thailand. It is found that WRF-MYNN2.5 produces a rainfall peak over the eastern Gulf of Thailand at about 1000–1300 LT, which is three hours later than that in TMPA. The rainfall peak over the western coastline of the Ca Mau Peninsula between 1300 and 1600 LT

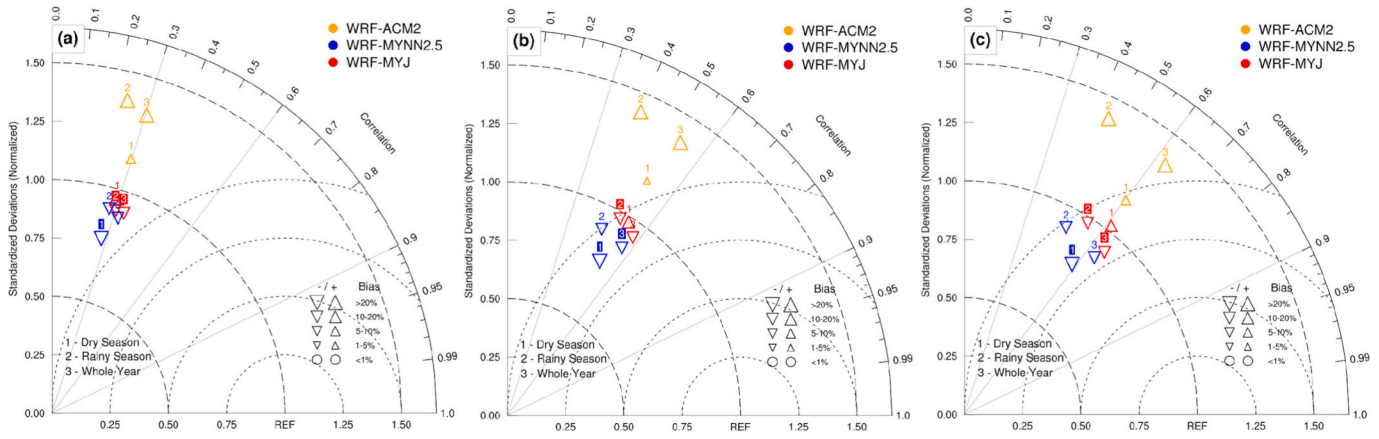

Fig. 7. The performance of WRF experiments employing different PBL parameterization schemes is assessed using Taylor diagrams for (a) daily, (b) 5-day, and (c) 10-day accumulated rainfall. Results are shown for the WRF-MYJ (red symbols), WRF-MYNN2.5 (blue symbols), and WRF-ACM2 (orange symbols) experiments across the dry season, rainy season, and full year for 2007, 2013, and 2015. Experiments with the smallest RMSE are highlighted with a colour-filled background of the numbers indicating the reference period. (For interpretation of the references to colour in this figure legend, the reader is referred to the web version of this article.)

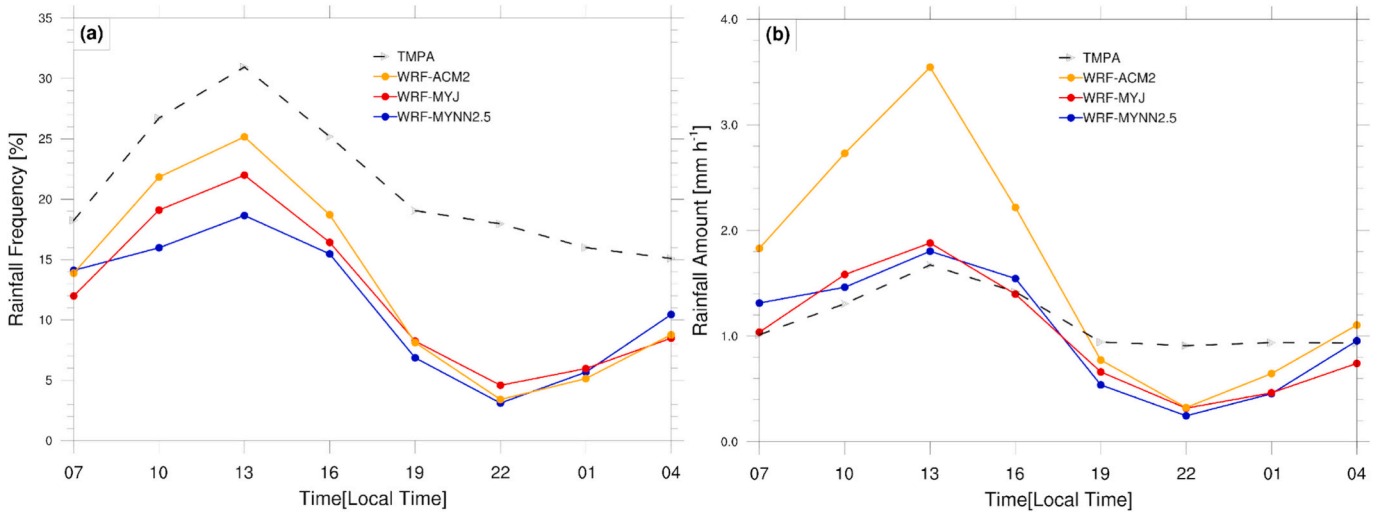

Fig. 8. Diurnal cycle of (a) rainfall frequency, and (b) rainfall amount averaged over the three southern provinces from TMPA (dashed black lines), WRF-ACM2 (orange lines), WRF-MYJ (red lines), and WRF-MYNN2.5 (blue lines) in the rainy seasons of 2007, 2013, and 2015. (For interpretation of the references to colour in this figure legend, the reader is referred to the web version of this article.)

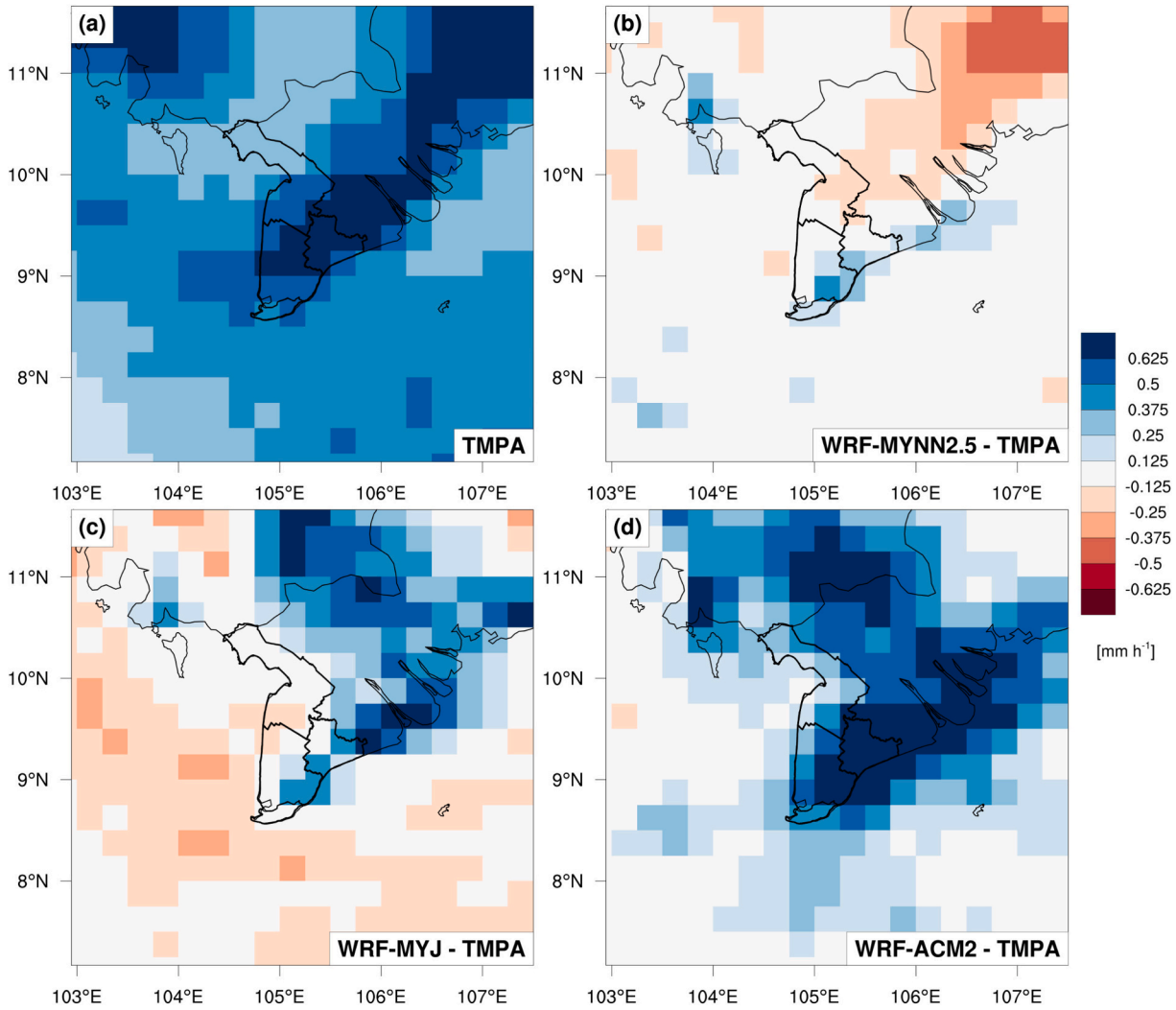

Fig. 9. (a) Mean 3-hourly TMPA rainfall intensity during the peak of the diurnal cycle (i.e., 13–16 LT) in the rainy seasons of 2007, 2013, and 2015. Difference between the mean 3-hourly rainfall intensity in the same period from (b) WRF-MYNN2.5, (c) WRF-MYJ, and (d) WRF-ACM2 experiments and the TMPA average shown in (a).

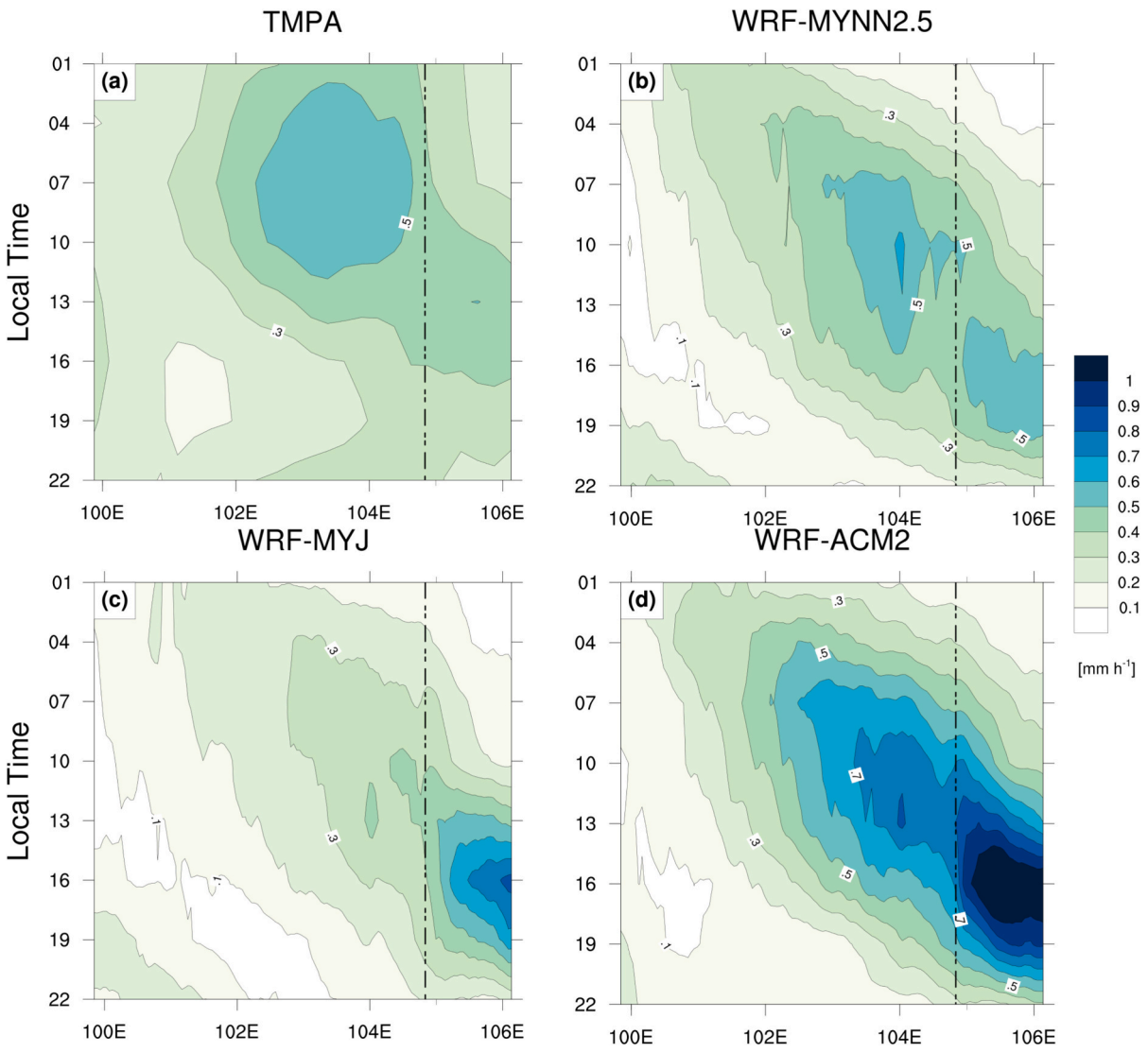

Fig. 10. Hovmöller diagrams of the mean diurnal cycles latitudinally averaged over 8.25–10.5°N, 99.875–106.125°E (see red rectangle in Fig. 1) for the rainy seasons in 2007, 2013, and 2015 from (a) TMPA, and from (b) WRF-MYNN2.5, (c) WRF-MYJ, and (d) WRF-ACM2 experiments. Vertical dashed lines show the approximate location of the western coastline of the Ca Mau Peninsula. (For interpretation of the references to colour in this figure legend, the reader is referred to the web version of this article.)

corresponds well with TMPA, and the inland propagation afterwards is reasonably captured. The overall magnitude of the diurnal cycle in WRF-MYNN2.5 is also close to the observed. On the other hand, both WRF-MYJ and WRF-ACM2 fail to capture the above-mentioned diurnal features. In particular, WRF-MYJ produces the early morning peak that is too weak over the eastern Gulf of Thailand (with the underestimation of about 0.2 mm h^{-1} compared to TMPA; Fig. 8c) and the early afternoon peak that is too strong overland (with the overestimation of about 0.2 mm h^{-1} compared to TMPA). Whereas, WRF-ACM2 produces a morning peak which is three hours earlier and stronger over the eastern Gulf of Thailand (with the overestimation of about 0.1 mm h^{-1} compared to TMPA; Fig. 8d), and the early afternoon peak is much stronger overland (with the overestimation of about 0.5 mm h^{-1} compared to TMPA). Compared to other experiments, it is obvious that WRF-MYNN2.5 outperforms the other simulations in capturing the diurnal rainfall over the Ca Mau Peninsula.

Additionally, we inspect the performance of all WRF experiments without using the sst_skin option for simulating diurnal cycle migration over the Ca Mau Peninsula during the rainy season (Fig. S4). Again, compared with experiments without using the sst_skin option, those using the sst_skin option simulate a more realistic magnitude of both the diurnal peak over the eastern Gulf of Thailand and overland. For instance, WRF-MYNN2.5-s produces an afternoon peak over the western coastline of the Ca Mau Peninsula, which is too early (1000–1300 LT; Fig. S4b), whereas WRF-MYNN2.5 is able to accurately capture this one (Fig. 10b). Likewise, WRF-ACM2-s (Fig. S4d) overestimates both the morning peak over the Gulf of Thailand by about 0.4 mm h-1 and the early afternoon peak overland by about 0.5 mm h-1, while WRF-ACM2 overestimates the morning peak by about 0.1 mm h-1 (Fig. 10d).

3.4. Role of the PBL parameterization schemes on simulated daily PET

This section attempts to attribute the differential performance between WRF simulations using different PBL parameterization schemes in simulating daily PET over the Ca Mau Peninsula. Figs. 11 and 12 show the PBIAS and RMSE of daily PET for simulations WRF-MYNN2.5, WRF-MYJ, and WRF-ACM2 for the period 2007–2013-2015 compared to ERA5. Yellow shading denotes ocean grid points, for which PET values are not available. While the WRF-MYNN2.5 experiment has a negative bias in both dry and rainy seasons, the other two experiments tend to

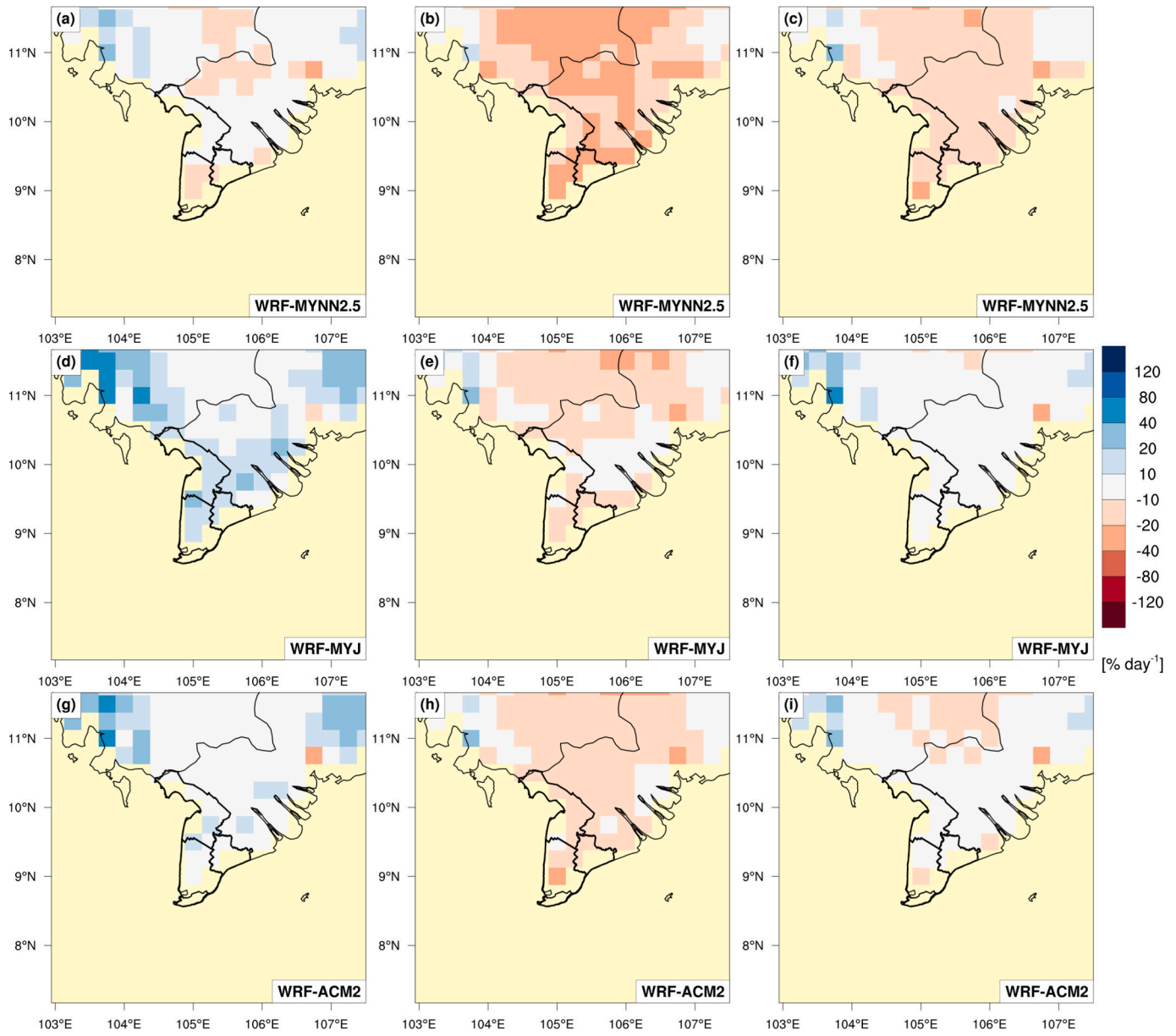

Fig. 11. Same as in Fig. 5 but for daily PET from the experiments compared to ERA5.
Yellow shading denotes ocean grid points, for which PET values are not available. (For interpretation of the references to colour in this figure legend, the reader is referred to the web version of this article.)

produce a positive bias in the rainy season and a negative bias in the dry season over the Ca Mau Peninsula. The RMSE of daily PET over the Ca Mau Peninsula in the dry season is greater than in the rainy season by all three experiments (see Table 3). Based on the RMSE, all three experiments exhibit comparable performances when compared with ERA5; the discrepancies are insignificant, with a maximum RMSE value of 1.33 mm day^{-1} and a minimum value of 1.29 mm day^{-1} (see Table 3).

Fig. 13 presents the Taylor diagram of daily PET at three stations over the Ca Mau Peninsula for simulations WRF-MYNN2.5, WRF-MYJ, and WRF-ACM2 for the period 2007–2013-2015, compared to PET calculated from the Penman-Monteith equation. Overall, all three experiments show better performance in the dry season compared to the rainy season, and exhibit negative biases (underestimation) in both seasons. The WRF-MYNN2.5 experiment exhibits the highest CC in both the dry season (about 0.65) and the rainy season (about 0.45). In addition, the WRF-MYNN2.5 experiment yields the smallest RMSE in both dry and rainy seasons, with values of approximately 1.25 mm day^{-1} in the rainy season and 1.15 mm day^{-1} in the dry season (see Table 3).

Wind speed at 10-m height and net radiation are the main variables that affect PET, and WRF-MYNN2.5 tends to simulate these values more accurately than WRF-MYJ and WRF-ACM2 (Table 4). The WRF-MYNN.2.5 experiment exhibits the smallest RMSE by 1.54 m s^{-1} on simulating wind speed at 10-m height, and 3.33 MJ m^{-2} on simulating net radiation. Generally, in both the rainy and dry seasons, net radiation is well simulated by all experiments, with the PBIAS ranging from −19 to 1%, and RMSE ranging from 3.27 to 3.97 MJ m^{-2}. However, all experiments have comparatively poor performance in simulating wind speed at 10-m height over the years, with PBIAS ranging from 51% to 66% during the rainy season and 73% to 87% during the dry season.

The high positive bias in wind speed at 10-m height, especially during the dry season, appears to be a major contributor to the bias in PET. We advocate the assumption that this bias is primarily driven by land-use data that is not properly considered by our WRF model setup. In

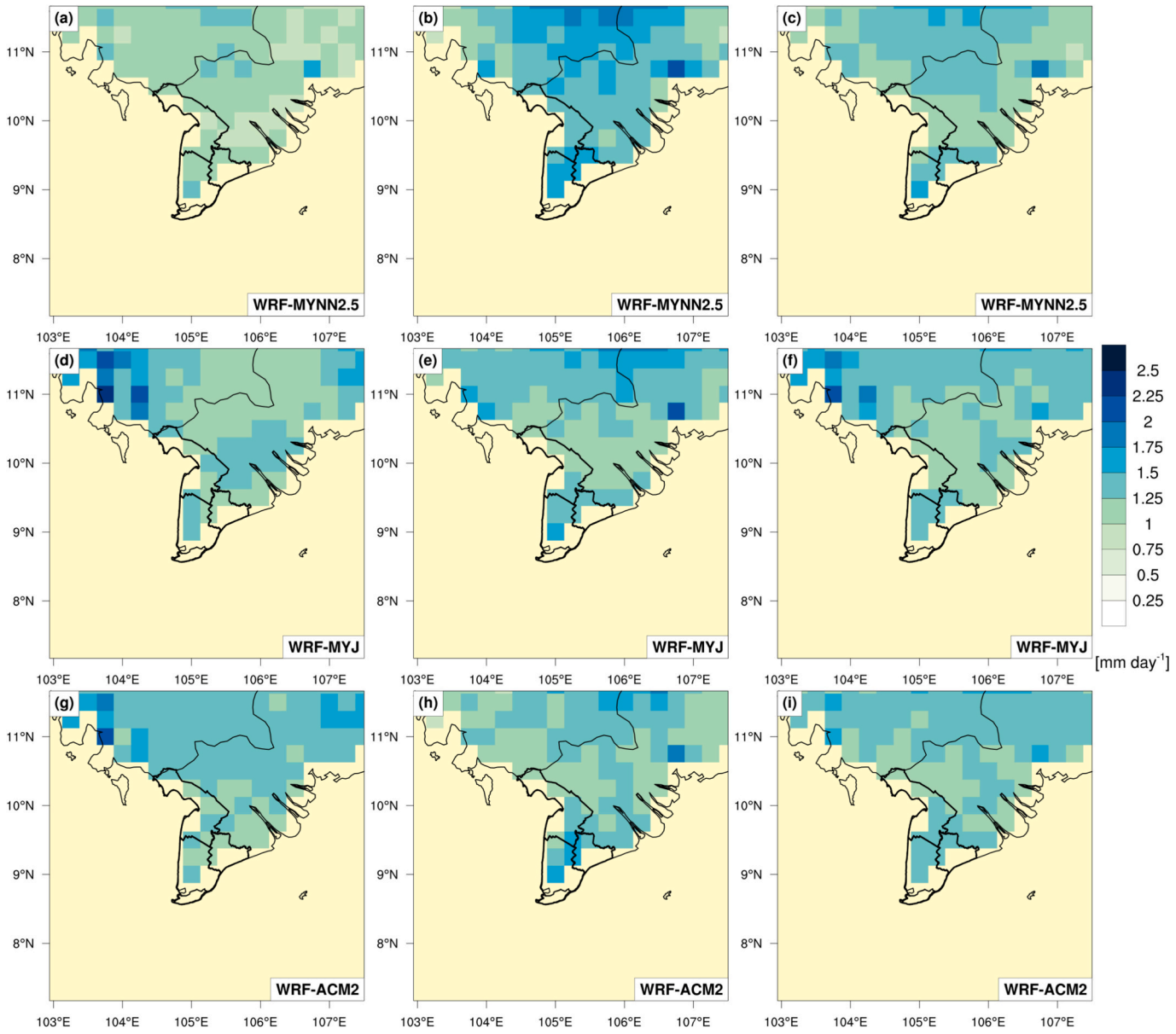

Fig. 12. Same as in Fig. 6 but for daily PET from the experiments compared to ERA5.
Yellow shading denotes ocean grid points, for which PET values are not available. (For interpretation of the references to colour in this figure legend, the reader is referred to the web version of this article.)

line with Xu et al. (2017) and Bughici et al. (2019), our results demonstrate that wind speed at 10-m height bias plays a crucial role in driving biases in simulated PET.

Table 3 also presents the PBIAS and RMSE of simulated PET from all experiments compared to GGI-3000 data at the two stations, Ca Mau and Can Tho. In the rainy season, the WRF-MYNN2.5 experiment generates the smallest RMSE (about 1.08 mm day^{-1}); meanwhile, in the dry season, the WRF-MYJ experiment exhibits the smallest RMSE (1.01 mm day^{-1}). In terms of the entire year, the WRF-MYNN2.5 experiment exhibits the best performance in simulating PET, with the smallest RMSE of 1.09 mm day^{-1}. In general, these results suggest that, similar to what is presented for precipitation, the WRF-MYNN2.5 experiment outperforms in capturing the PET over the Ca Mau Peninsula.

3.5. Physical mechanisms of PBL and SST sensitivity

The statistical results indicate that MYNN2.5, particularly when combined with the sst_skin option, provides the most realistic simulation of precipitation and PET over the Ca Mau Peninsula. To provide a physically grounded interpretation of these differences, this section links the model behavior to established quantitative findings on boundary-layer turbulence, moisture transport, and coastal convection processes.

Turbulent mixing within the planetary boundary layer governs the vertical transport of heat, moisture, and momentum and is typically parameterized using eddy-diffusivity formulations (Shin and Dudhia, 2016). Differences among PBL schemes, therefore, correspond to differences in effective turbulent diffusivity and mixing depth. Observationally constrained simulations over tropical sites have shown that variations in PBL parameterization can produce differences of several hundred meters in boundary-layer height and substantial changes in surface fluxes and vertical profiles of temperature and humidity (Hariprasad et al., 2014).

The primary structural distinction among the schemes considered here lies in the representation of vertical transport. MYNN2.5 and MYJ are local TKE-based schemes, in which turbulent fluxes depend on local gradients and prognosed turbulence, thereby limiting vertical exchange

Table 3
PBIAS and RMSE of simulated daily PET compared to station data (Penman-Monteith and GGI-3000) and ERA5 over the Ca Mau Peninsula in 2007, 2013, and 2015. Bold numbers indicate experiments with the lowest values of RMSE for each time period.

Experiment Name	WRF-MYNN2.5	WRF-MYJ	WRF-ACM2	WRF-MYNN2.5	WRF-MYJ	WRF-ACM2
	PBIAS (%)			RMSE (mm)		
Stations (Penman-Monteith)						
Rainy season	−14.13	−8.79	−4.15	1.26	1.42	1.31
Dry season	−14.47	−16.25	−8.65	1.15	1.41	1.17
Year	−14.30	−12.64	−6.47	1.21	1.42	1.24
Stations (GGI-3000)						
Rainy season	−7.90	15.00	5.89	1.08	1.32	1.35
Dry season	−15.21	−4.62	−7.70	1.11	1.01	1.15
Year	−11.79	4.55	−1.35	1.09	1.17	1.25
ERA5						
Rainy season	−7.85	14.57	5.23	1.09	1.27	1.26
Dry season	−21.33	11.41	−15.19	1.50	1.31	1.40
Year	−15.31	0.20	−6.06	1.31	1.29	1.33

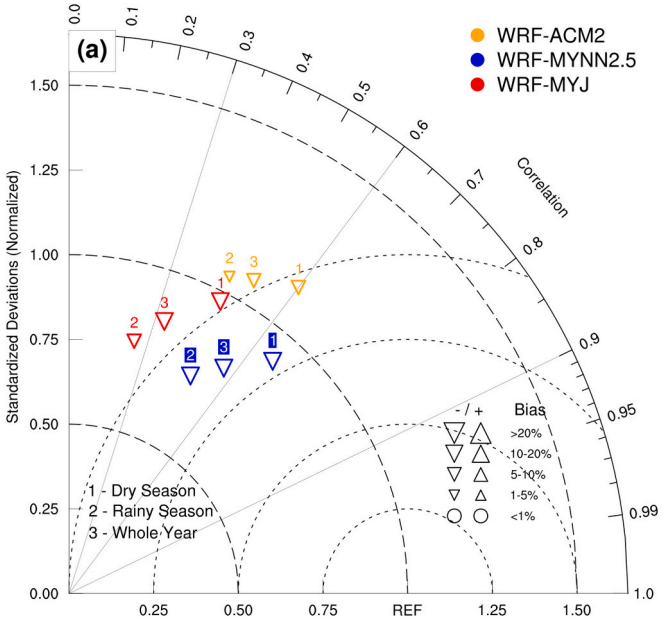

Fig. 13. Taylor diagram of daily PET for experiments WRF-MYJ (red symbols), WRF-MYNN2.5 (blue symbols), and WRF-ACM2 (orange symbols) at three stations over the Ca Mau Peninsula in the dry seasons, rainy seasons, and whole years in 2007, 2013, and 2015. Experiments with the smallest RMSE are highlighted with a colour-filled background of the numbers indicating the reference period. (For interpretation of the references to colour in this figure legend, the reader is referred to the web version of this article.)

between adjacent layers. In contrast, ACM2 includes a non-local component that permits vertically coherent transport across the full boundary-layer depth. Previous studies over the Asian monsoon region have quantified that such non-local mixing can increase boundary-layer depth and enhance upward moisture transport into the lower free troposphere, leading to higher moist static energy and stronger convective instability (Wang et al., 2014; Que et al., 2016; Jia et al., 2023).

These differences in turbulent transport provide a physically consistent explanation for the precipitation biases identified in this study. Over the Ca Mau Peninsula, the ACM2 configuration produces a substantial wet bias and higher RMSE relative to MYNN2.5, particularly during the rainy season. Enhanced vertical mixing in ACM2 likely increases the vertical flux of moisture and heat, promoting greater convective available potential energy (CAPE) and intensifying precipitation. In contrast, MYNN2.5 constrains vertical redistribution more effectively, limiting excessive moisture accumulation in the lower troposphere and yielding precipitation closer to observations. Similar relationships between mixing intensity, moisture profiles, and convective rainfall have been quantitatively demonstrated in previous WRF model studies (Hariprasad et al., 2014; Que et al., 2016).

Table 4
PBIAS and RMSE of simulated daily 10-m wind speed and net radiation compared to station data over the Ca Mau Peninsula in 2007, 2013, and 2015. Bold numbers indicate experiments with the lowest values of RMSE for each time period.

Experiment Name	WRF-MYNN2.5	WRF-MYJ	WRF-ACM2	WRF-MYNN2.5	WRF-MYJ	WRF-ACM2
10-m wind speed	PBIAS (%)			RMSE ($m\ s^{-1}$)		
Rainy season	51.10	66.44	56.04	1.48	1.84	1.64
Dry season	73.89	87.70	82.51	1.59	1.87	1.74
Year	61.48	76.12	68.09	1.54	1.85	1.69
Daily net radiation	PBIAS (%)			RMSE ($MJ\ m^{-2}$)		
Rainy season	−10.87	−2.87	1.0	3.27	3.79	3.63
Dry season	−19.01	−15.71	−11.63	3.39	3.97	3.40
Year	−15.04	−9.45	−5.45	3.33	3.87	3.52

The influence of PBL formulation is further amplified by the coastal setting of the Ca Mau Peninsula. Coastal rainfall systems are strongly modulated by land–sea interactions, which can account for a substantial fraction of total precipitation in tropical regions (Bergemann et al., 2015; Bergemann and Jakob, 2016; Zhu et al., 2017). In such environments, turbulent mixing interacts with mesoscale circulations, including boundary-layer jets and sea–land breeze systems. Recent studies over the East Sea (South China Sea) in Vietnam have shown that variations in PBL mixing can alter boundary-layer jet strength and low-level moisture convergence, leading to significant differences in coastal precipitation (Wang et al., 2014; Shen and Du, 2023). In addition, PBL schemes have been shown to modify the timing and intensity of sea–land breeze circulations, thereby influencing the diurnal cycle of convection (He et al., 2022). The diurnal characteristics of precipitation in the present simulations are consistent with these mechanisms. During the peak convective period (1300–1600 LT), WRF-ACM2 exhibits a substantially stronger overestimation of rainfall intensity than WRF-MYNN2.5. This behavior is consistent with enhanced moisture transport and convective amplification under stronger mixing conditions, as documented in previous monsoon studies (Wang et al., 2014; Que et al., 2016; Qian et al., 2016), where differences in vertical moisture flux were directly linked to differences in precipitation intensity.

Surface energy processes provide an additional pathway by which PBL formulation affects precipitation. Stronger vertical mixing, especially in non-local schemes, can enhance upward latent heat flux over warm ocean surfaces and thereby increase moisture supply to the boundary layer (Cha et al., 2008; Qian et al., 2016). In simulations with prescribed SST, this enhanced evaporative forcing is not compensated by ocean cooling, which may sustain excessive moisture supply and amplify convective rainfall through a positive feedback (Wang et al., 2014; Cha et al., 2008). The sst_skin option partly alleviates this limitation by allowing the skin temperature to respond to radiative forcing and turbulent exchange, thereby modifying surface heat flux partitioning (Zeng and Beljaars, 2005; Brunke et al., 2008; Shi et al., 2024). The 10–40% reduction in precipitation bias after activating sst_skin (Section

3.1; Fig. 4) therefore suggests that part of the bias in the sst_skin-off experiments arises from unresolved air–sea thermodynamic coupling, consistent with previous studies showing that diurnal SST variability modulates surface turbulent fluxes and convection in tropical and coastal environments (Seo et al., 2014; Senatore et al., 2014; Busquets et al., 2025).

Overall, the results can be understood as a coherent process chain linking PBL mixing intensity, vertical moisture transport, convective instability, coastal circulation dynamics, and surface energy feedbacks. The improved performance of MYNN2.5 suggests that it provides a more balanced representation of these coupled processes in a tropical coastal environment.

4. Conclusions

In this study, we investigated the sensitivity of daily precipitation, the diurnal cycle of precipitation, and daily PET to the PBL parameterization scheme and the sst_skin option (which allows diurnally varying SST calculations) in the WRF model over the Ca Mau Peninsula, with a key strength being the use of fairly dense in-situ station observations as a reliable reference for evaluation. The overarching objective was to identify an optimal combination of physics parameterizations capable of reliably simulating the regional freshwater flux. To our knowledge, this study represents the first attempt to simultaneously simulate both rainfall and PET for the Ca Mau Peninsula using gray-zone (5 km) WRF experiments. The principal findings of this work can be summarized as follows:

1) The results for simulating daily precipitation are similar using local closure PBL schemes, including MYJ and MYNN2.5. These two local closure schemes better represent the precipitation observations compared to the non-local closure ACM2 scheme. In the dry season, the spatial distribution from both experiments is better than that in the rainy season. During the rainy season, dry biases prevail for the MYJ and MYNN2.5 schemes over the Ca Mau Peninsula and the surrounding sea, while ACM2 leads to wet biases over the Ca Mau Peninsula. Although the non-local ACM2 scheme has been shown to outperform local-closure schemes in simulating precipitation over several regions (Meroni et al., 2021; Huang et al., 2023; Reddy et al., 2023), its application over the Ca Mau Peninsula proves unsatisfactory, as it consistently overestimates rainfall in both seasons. With respect to the sst_skin option, the results suggest that increasing the temporal resolution of the SST variable by activating this option may diminish the biases caused by the PBL parameterization scheme over not only the Ca Mau Peninsula but also the surrounding ocean. By using this option in conjunction with the MYNN2.5 scheme, the PBIAS could be reduced by 10–40% in the Ca Mau Peninsula region.
2) Regarding the diurnal cycle of precipitation, gray-zone WRF experiments can reasonably reproduce its characteristics in the Ca Mau Peninsula. However, the rainfall frequency and rainfall amount in all runs are noticeably underestimated at night (1900–0400 LT). The WRF-MYNN2.5 experiment can produce a diurnal rainfall peak near the coast of the Ca Mau Peninsula (approximately 200 km from the western coastline) with a magnitude similar to the observed one. The inland rainfall peak in the early afternoon was also captured in the WRF-MYNN2.5 simulations. Conversely, the WRF-MYJ and WRF-ACM2 experiments produce a morning peak near the seaside of Ca Mau Peninsula that is too early, and the inland afternoon peak is too strong, independently of the sst_skin option.
3) In terms of PET, performance indicator results reveal WRF-MYNN2.5 as the best performer. The wind speed at 10-m height was the major contributor to the PET bias in our study.

The above-mentioned findings suggest that the choice of the PBL parameterization scheme and the sst_skin option has a fairly positive impact on the freshwater flux simulation over the Ca Mau Peninsula. Among the tested experiments, the WRF–MYNN2.5 scheme combined with the activation of the sst_skin option yields the most accurate representation of freshwater flux over the Ca Mau Peninsula and therefore constitutes the most appropriate choice for subsequent investigations. These results are similar to those of Lai et al. (2025), who demonstrated that in gray-zone simulations of the Indian summer monsoon, rainfall sensitivity was significantly influenced by the selection of the PBL scheme, while changes in microphysics had a comparatively minor effect. It should be noted, however, that this interpretation remains literature-based rather than directly diagnosed from model output. Future work should explicitly analyze boundary-layer depth, vertical moisture fluxes, and turbulence-related variables to further quantify the mechanisms inferred here.

Under global warming, spatial and temporal variability in freshwater flux is projected to intensify, reinforcing the paradigm of “wet gets wetter, dry gets drier” (Chou et al., 2013; Byrne and O'Gorman, 2015; Ficklin et al., 2022; Allan, 2023). Such changes carry profound implications for human livelihoods, socioeconomic development, and ecosystem resilience (Allan et al., 2020; Huggins et al., 2022), particularly in regions such as the Ca Mau Peninsula, where aquaculture and agriculture are dominant. To cope with these changes, a solid understanding of the freshwater flux over the Ca Mau Peninsula is required. This study, thus, can provide important guidelines for understanding the sensitivity of two components of the freshwater flux, including precipitation and PET, to physical parameterization in gray-zone scales (5 km) RCMs. The model demonstrates encouraging skill in reproducing the diurnal cycle of precipitation and daily PET, though its performance in simulating daily precipitation remains more limited. Building on these results, a decade-long simulation is planned to provide a more comprehensive perspective on freshwater flux over the Ca Mau Peninsula. Additionally, land-use change emerges as a key factor that warrants further investigation. The rapid expansion of aquaculture since 2000 has transformed land-use over the Ca Mau Peninsula (Phan et al., 2021), potentially altering near-surface wind speeds, a primary driver of PET biases. Incorporating land-use change into future simulations will therefore be crucial for refining the assessment of freshwater flux in this vulnerable region.

CRediT authorship contribution statement

Duc Tran-Anh: Writing – original draft, Validation, Methodology, Data curation, Conceptualization. **Andreas H. Fink:** Writing – review & editing, Validation, Methodology, Conceptualization. **Patrick Laux:** Writing – review & editing, Methodology, Conceptualization. **Joël Arnault:** Writing – review & editing, Visualization, Validation, Data curation. **Harald Kunstmann:** Writing – review & editing, Methodology, Conceptualization. **Tan Phan-Van:** Writing – review & editing, Supervision, Conceptualization. **Roderick van der Linden:** Writing – review & editing, Visualization, Validation, Supervision, Conceptualization.

Declaration of competing interest

None.

Acknowledgments

The simulations were conducted at the KIT's high-performance computing system HoreKa in Karlsruhe. The observational data over the Ca Mau Peninsula were provided by the National Centre for Hydro-Meteorological Forecasting of Vietnam. Special thanks go to the KAAD scholarship fund and the ViWat Mekong; Integrated Solutions for Sustainable Development in the Mekong Delta –Land, Water, Energy and Climate – Sub-project 1 ViWat Engineering under the BMBF grant 02WCL1474A.

Appendix A. Supplementary data

Supplementary data to this article can be found online at https://doi.org/10.1016/j.atmosres.2026.109029.

Data availability

All data used in this study are openly available and can be freely downloaded from: 1) The 3-hourly TMPA global rainfall dataset: https://disc.gsfc.nasa.gov/datasets/TRMM_3B42_7/. 2) The daily CHIRPS v2.0 rainfall dataset: https://data.chc.ucsb.edu/products/CHIRPS-2.0/. 3) Monthly Oceanic Niño Index: https://origin.cpc.ncep.noaa.gov/products/analysis_monitoring/ensostuff/ONI_v5.php. 4) The hourly ERA-5 reanalysis dataset: https://cds.climate.copernicus.eu/datasets/reanalysis-era5-single-levels?tab=download.

References

Abatzoglou, J.T., Dobrowski, S.Z., Parks, S.A., Hegewisch, K.C., 2018. TerraClimate, a high-resolution global dataset of monthly climate and climatic water balance from 1958–2015. Sci. Data 5, 170191. https://doi.org/10.1038/sdata.2017.191.

Allan, R.P., 2023. Amplified seasonal range in precipitation minus evaporation. Environ. Res. Lett. 18, 094004. https://doi.org/10.1088/1748-9326/acea36.

Allan, R.P., Barlow, M., Byrne, M.P., Cherchi, A., Douville, H., Fowler, H.J., Gan, T.Y., Pendergrass, A.G., Rosenfeld, D., Swann, A.L.S., Wilcox, L.J., Zolina, O., 2020. Advances in understanding large-scale responses of the water cycle to climate change. Ann. N. Y. Acad. Sci. 1472, 49–75. https://doi.org/10.1111/nyas.14337.

Bergemann, M., Jakob, C., 2016. How important is tropospheric humidity for coastal rainfall in the tropics? Geophys. Res. Lett. 43 (11), 5860–5868. https://doi.org/10.1002/2016GL069255.

Bergemann, M.M., Jakob, C., Lane, T.P., 2015. Global detection and analysis of coastline-associated rainfall using an objective pattern recognition technique. J. Clim. 28 (18), 7225–7236. https://doi.org/10.1175/JCLI-D-15-0098.1.

Brunke, M.A., Zeng, X., Misra, V., Beljaars, A., 2008. Integration of a prognostic sea surface skin temperature scheme into weather and climate models. J. Geophys. Res. Atmos. 113, D21117. https://doi.org/10.1029/2008JD010607.

Bughici, T., Lazarovitch, N., Fredj, E., Tas, E., 2019. Evaluation and bias correction in WRF model forecasting of precipitation and potential evapotranspiration. J. Hydrometeorol. 20, 1453–1471. https://doi.org/10.1175/JHM-D-18-0160.1.

Busquets, E., Udina, M., Bech, J., Mercader, J., 2025. Sea surface temperature updating impacts on WRF simulations during a heatwave period. Atmos. Res. 326, 108230. https://doi.org/10.1016/j.atmosres.2025.108230.

Byrne, M.P., O'Gorman, P.A., 2015. The response of precipitation minus evapotranspiration to climate warming: why the "wet-get-wetter, dry-get-drier" scaling does not hold over land. J. Clim. 28, 8078–8092. https://doi.org/10.1175/JCLI-D-15-0369.1.

Cha, D.-H., Lee, D.-K., Hong, S.-Y., 2008. Impact of boundary layer processes on seasonal simulation of the East Asian summer monsoon using a regional climate model. Meteorog. Atmos. Phys. 100, 53–72. https://doi.org/10.1007/s00703-008-0295-6.

Chen, G., 2020. Diurnal cycle of the Asian summer monsoon: air pump of the second kind. J. Clim. 33, 1747–1775. https://doi.org/10.1175/JCLI-D-19-0210.1.

Chen, X., Pauluis, O.M., Zhang, F., 2018. Regional simulation of Indian summer monsoon intraseasonal oscillations at gray-zone resolution. Atmos. Chem. Phys. 18, 1003–1022. https://doi.org/10.5194/acp-18-1003-2018.

Chou, C., Tu, J.-Y., Tan, P.-H., 2013. Increase in the range between wet and dry season precipitation. Nat. Geosci. 6, 263–267. https://doi.org/10.1038/ngeo1744.

Clayson, C.A., Bogdanoff, A.S., 2015. The effect of diurnal sea surface temperature warming on climatological air–sea fluxes. J. Clim. 28, 2546–2556. https://doi.org/10.1175/JCLI-D-12-00062.1.

Climate Prediction Center (CPC), NOAA, 2025. NOAA's Climate Prediction Center. Available online at https://origin.cpc.ncep.noaa.gov/products/analysis_monitoring/ensostuff/ONI_v5.php (accessed 15 January 2025).

Dai, A., 2011. Characteristics and trends in various forms of the palmer drought severity index during 1900–2008. J. Geophys. Res. Atmos. 116, D12115. https://doi.org/10.1029/2010JD015541.

Dang, V.H., Tran, D.D., Cham, D.D., Hang, P.T.T., Nguyen, H.T., Truong, H.V., Tran, P. H., Duong, M.B., Nguyen, N.T., Le, K.V., et al., 2020. Assessment of rainfall distributions and characteristics in coastal provinces of the Vietnamese Mekong Delta under climate change and ENSO processes. Water 12, 1555. https://doi.org/10.3390/w12061555.

Dinh, K.D., Anh, T.N., Nguyen, N.Y., Bui, D.D., Srinivasan, R., 2020. Evaluation of grid-based rainfall products and water balances over the Mekong river basin. Remote Sens. 12, 1858. https://doi.org/10.3390/rs12111858.

Donohue, R.J., McVicar, T.R., Roderick, M.L., 2010. Assessing the ability of potential evaporation formulations to capture the dynamics in evaporative demand within a changing climate. J. Hydrol. 386, 186–197. https://doi.org/10.1016/j.jhydrol.2010.03.020.

Duan, Z., Liu, J., Tuo, Y., Chiogna, G., Disse, M., 2016. Evaluation of eight high spatial resolution gridded precipitation products in Adige Basin (Italy) at multiple temporal and spatial scales. Sci. Total Environ. 573, 1536–1553. https://doi.org/10.1016/j.scitotenv.2016.08.213.

Duc, H.N., Bang, H.Q., Quang, N.X., 2018. Influence of the pacific and Indian Ocean climate drivers on the rainfall in Vietnam. Int. J. Climatol. 38, 5717–5732. https://doi.org/10.1002/joc.5774.

Dudhia, J., 1989. Numerical study of convection observed during the winter monsoon experiment using a mesoscale two-dimensional model. Mon. Weather Rev. 117, 262–278. https://doi.org/10.1175/1520-0469(1989)046<3077:NSOCOD>2.0.CO;2.

Dzebre, D.E.K., Adaramola, M.S., 2020. A preliminary sensitivity study of planetary boundary layer parameterisation schemes in the weather research and forecasting model to surface winds in coastal Ghana. Renew. Energy 146, 66–86. https://doi.org/10.1016/j.renene.2019.06.133.

Ficklin, D.L., Null, S.E., Abatzoglou, J.T., Novick, K.A., Myers, D.T., 2022. Hydrological intensification will increase the complexity of water resource management. Earth's Future 10, e2021EF002487. https://doi.org/10.1029/2021EF002487.

Fu, Y., Xie, S.-P., Xu, C.-Y., Deng, Q., 2023. Climate change projection over mainland Southeast Asia and the Lancang–Mekong River Basin based on a set of RegCM4 simulations. Int. J. Climatol. 43, 842–860. https://doi.org/10.1002/joc.7811.

Funk, C., Peterson, P., Landsfeld, M., Pedreros, D., Verdin, J., Shukla, S., Husak, G., Rowland, J., Harrison, L., Hoell, A., Michaelsen, J., 2015. The climate hazards infrared precipitation with stations - a new environmental record for monitoring extremes. Sci. Data 2, 150066. https://doi.org/10.1038/sdata.2015.66.

Gao, X., Zhao, Z., Ding, Y., Huang, R., Giorgi, F., 2001. Climate change due to greenhouse effects in China as simulated by a regional climate model. Adv. Atmos. Sci. 18, 1224–1230. https://doi.org/10.1007/s00376-001-0036-y.

Garratt, J.R., 1994. The atmospheric boundary layer. Earth Sci. Rev. 37, 89–134. https://doi.org/10.1016/0012-8252(94)90026-4.

Gelaro, R., McCarty, W., Suárez, M.J., Todling, R., Molod, A., Takacs, L., Randles, C., Darmenov, A., Bosilovich, M.G., Reichle, R., Wargan, K., et al., 2017. The Modern-Era retrospective analysis for research and applications, version 2 (MERRA-2). J. Clim. 30, 5419–5454. https://doi.org/10.1175/JCLI-D-16-0758.1.

General Statistics Office of Vietnam (GSO), 2019. Statistical Yearbook of Vietnam. Statistical Publishing House, Hanoi, Vietnam.

Gholami, S., Ghader, S., Khaleghi-Zavareh, H., Ghafarian, P., 2021. Sensitivity of WRF-simulated 10 m wind over the Persian Gulf to different boundary conditions and planetary boundary layer parameterization schemes. Atmos. Res. 247, 105147. https://doi.org/10.1016/j.atmosres.2020.105147.

Giorgi, F., 1990. Simulation of regional climate using a limited area model nested in a general circulation model. J. Clim. 3, 941–963. https://doi.org/10.1175/1520-0442(1990)003<0941:SORCUA>2.0.CO;2.

Giorgi, F., Torma, C., Coppola, E., Ban, N., Schär, C., Somot, S., 2016. Enhanced summer convective rainfall at alpine high elevations in response to climate warming. Nat. Geosci. 9, 584–589. https://doi.org/10.1038/ngeo2761.

Grell, G.A., Devenyi, D., 2002. A generalized approach to parameterizing convection combining ensemble and data assimilation techniques. Geophys. Res. Lett. 29, 1693. https://doi.org/10.1029/2002GL015311.

Grell, G.A., Freitas, S.R., 2014. A scale- and aerosol-aware stochastic convective parameterization for weather and air quality modeling. Atmos. Chem. Phys. 14, 5233–5250. https://doi.org/10.5194/acp-14-5233-2014.

Guo, H., Bao, A., Liu, T., Ndayisaba, F., He, D., Kurban, A., De Maeyer, P., 2017. Meteorological drought analysis in the lower Mekong basin using the satellite-based long-term CHIRPS product. Sustainability 9, 901. https://doi.org/10.3390/su9060901.

Ha, T.T.P., van Dijk, H., Bosma, R.H., Sinh, L.X., 2013. Livelihood capabilities and pathways of shrimp farmers in the Mekong delta, Vietnam. Aquac. Econ. Manag. 17, 1–30. https://doi.org/10.1080/13657305.2013.747224.

Hariprasad, K.B.R.R., Srinivas, C.V., Singh, A.B., Rao, S.V.B., Baskaran, R., Venkatraman, B., 2014. Numerical simulation and intercomparison of boundary layer structure with different PBL schemes in WRF using experimental observations at a tropical site. Atmos. Res. 145–146, 27–44. https://doi.org/10.1016/j.atmosres.2014.03.023.

He, J., Zhang, Y., Liu, Y., et al., 2022. Adaptability evaluation of boundary layer schemes for simulation of sea and land breeze circulation in the west coast of the yellow sea. Atmos. Res. 278, 106354. https://doi.org/10.1016/j.atmosres.2022.106354.

Hentgen, L., Ban, N., Kröner, N., Leutwyler, D., Schär, C., 2019. Clouds in convection-resolving climate simulations over Europe. J. Geophys. Res. Atmos. 124, 3849–3870. https://doi.org/10.1029/2018JD030150.

Hersbach, H., Bell, B., Berrisford, P., Hirahara, S., Horányi, A., Muñoz-Sabater, J., Nicolas, J., Peubey, C., Radu, R., Schepers, D., et al., 2020. The ERA5 global reanalysis. Q. J. R. Meteorol. Soc. 146, 1999–2049. https://doi.org/10.1002/qj.3803.

Hersbach, H., Bell, B., Berrisford, P., Biavati, G., Horányi, A., Muñoz-Sabater, J., Nicolas, J., Peubey, C., Radu, R., Rozum, I., et al., 2023. ERA5 monthly averaged data on pressure levels from 1940 to present. In: Copernicus Climate Change Service (C3S) Climate Data Store. https://doi.org/10.24381/cds.f17050d7 (accessed March 2025).

Hoang-Cong, H., Ngo-Duc, T., Nguyen-Thi, T., Trinh-Tuan, L., Chung, J.X., Tangang, F., et al., 2022. A high-resolution climate experiment over part of Vietnam and the lower Mekong basin: performance evaluation and projection for rainfall. Vietnam J. Earth Sci. 44, 92–108. https://doi.org/10.15625/2615-9783/16942.

Hong, S.-Y., Lim, J.-O.J., 2006. The WRF single-moment 6-class microphysics scheme (WSM6). Asia-Pac. J. Atmos. Sci. 42, 129–151.

Hou, A.Y., Kakar, R.K., Neeck, S., Azarbarzin, A.A., Kummerow, C.D., Kojima, M., Iguchi, T., Oki, R., Nakamura, K., 2014. The global precipitation measurement mission. Bull. Am. Meteorol. Soc. 95, 701–722. https://doi.org/10.1175/BAMS-D-13-00164.1.

Hu, X.-M., Nielsen-Gammon, J.W., Zhang, F., 2010. Evaluation of three planetary boundary layer schemes in the WRF model. J. Appl. Meteorol. Climatol. 49, 1831–1844. https://doi.org/10.1175/2010JAMC2432.1.

Huang, Y., Xue, M., Hu, X., Martin, E., Novoa, H.M., McPherson, R.A., Perez, A., Morales, I.Y., 2023. Convection-permitting simulations of precipitation over the Peruvian Central Andes: strong sensitivity to planetary boundary layer parameterization. J. Hydrometeorol. 24, 1969–1990. https://doi.org/10.1175/JHM-D-22-0173.1.

Huffman, G.J., Bolvin, D.T., 2014. TRMM and Other Data Precipitation Data Set Documentation. NASA Goddard Space Flight Center, p. 42. Available online at https://pmm.nasa.gov/sites/default/files/document_files/3B42_3B43_doc_V7.pdf (accessed March 2025).

Huggins, X., Gleeson, T., Kummu, M., Zipper, S.C., Wada, Y., Troy, T.J., Famiglietti, J.S., 2022. Hotspots for social and ecological impacts from freshwater stress and storage loss. Nat. Commun. 13, 439. https://doi.org/10.1038/s41467-022-28029-w.

Intergovernmental Panel on Climate Change (IPCC), 2014. Climate Change 2014: Impacts, Adaptation, and Vulnerability. Contribution of Working Group II to the Fifth Assessment Report of the Intergovernmental Panel on Climate Change. Cambridge University Press, Cambridge, p. 1132.

Janjić, Z.I., 1994. The step-mountain eta coordinate model: further developments of the convection, viscous sublayer, and turbulence closure schemes. Mon. Weather Rev. 122, 927–945. https://doi.org/10.1175/1520-0493(1994)122<0927:TSMECM>2.0.CO;2.

Jia, W., Zhang, X., Wang, H., Wang, Y., Wang, D., Zhong, J., Zhang, W., Zhang, L., Guo, L., Lei, Y., Wang, J., Yang, Y., Lin, Y., 2023. Comprehensive evaluation of typical planetary boundary layer (PBL) parameterization schemes in China – part 1: Understanding expressiveness of schemes for different regions from the mechanism perspective. Geosci. Model Dev. 16, 6635–6670. https://doi.org/10.5194/gmd-16-6635-2023.

Jiang, C., Nie, Z., Mu, X., Wang, F., Liu, W., 2016. Potential evapotranspiration change and its attribution in the Qinling Mountains and surrounding area, China, during 1960–2012. J. Water Clim. Change 7, 526–541. https://doi.org/10.2166/wcc.2016.110.

Jiang, Z., Raghavan, S.V., Hur, J., Sun, Y., Liong, S.-Y., Nguyen, V.Q., Dang, T.P., 2019. Future changes in rice yields over the Mekong river delta due to climate change—alarming or alerting? Theor. Appl. Climatol. 137, 545–555. https://doi.org/10.1007/s00704-018-2617-z.

Jin, E.K., Choi, I.J., Kim, S.Y., Han, J.Y., 2016. Impact of model resolution on the simulation of diurnal variations of precipitation over East Asia. J. Geophys. Res. Atmos. 121, 1652–1670. https://doi.org/10.1002/2015JD023948.

Jones, P.W., 1999. First- and second-order conservative remapping schemes for grids in spherical coordinates. Mon. Weather Rev. 127, 2204–2210. https://doi.org/10.1175/1520-0493(1999)127<2204:FASOCR>2.0.CO;2.

Kaveney, B., Barrett-Lennard, E., Minh, K.C., Dang, M.D., Nguyen Thi, K.P., Kristiansen, P., Orgill, S., Stewart-Koster, B., Condon, J., 2023. Inland dry season saline intrusion in the Vietnamese Mekong River delta is driving the identification and implementation of alternative crops to rice. Agric. Syst. 207, 103632. https://doi.org/10.1016/j.agsy.2023.103632.

Kendon, E.J., Prein, A.F., Senior, C.A., Stirling, A., 2021. Challenges and outlook for convection-permitting climate modelling. Philos. Trans. R. Soc. A Math. Phys. Eng. Sci. 379, 20190547. https://doi.org/10.1098/rsta.2019.0547.

Kobayashi, S., Ota, Y., Harada, Y., Ebita, A., Moriya, M., Onoda, H., et al., 2015. The JRA-55 reanalysis: general specifications and basic characteristics. J. Meteorol. Soc. Japan. Ser. II 93, 5–48. https://doi.org/10.2151/jmsj.2015-001.

Kohut, M., Rožnovský, J., Knozová, G., 2014. Comparison of actual evaporation from water surface measured by GGI-3000 evaporimeter with values calculated by the penman equation. Contrib. Geophys. Geodesy 44, 231–240. https://doi.org/10.1515/congeo-2015-0003.

Koo, M.-S., Hong, S.-Y., 2010. Diurnal variations of simulated precipitation over East Asia in two regional climate models. J. Geophys. Res. Atmos. 115, D05105. https://doi.org/10.1029/2009JD012574.

Kwon, Y.-C., Hong, S.-Y., 2017. A mass-flux cumulus parameterization scheme across gray-zone resolutions. Mon. Weather Rev. 145, 583–598. https://doi.org/10.1175/MWR-D-16-0034.1.

Lai, H.-W., Ou, T., Dai, A., Chen, X., Chen, A., 2025. Diurnal cycle of summer precipitation over mainland Southeast Asia revealed by observations, reanalysis, and dynamic downscaling. J. Geophys. Res. Atmos. 130, e2024JD043020. https://doi.org/10.1029/2024JD043020.

Laux, P., Phan, V.T., Lorenz, C., Thuc, T., Ribbe, L., Kunstmann, H., 2013. Setting up regional climate simulations for Southeast Asia. In: High Performance Computing in Science and Engineering '12. Springer, Berlin, Heidelberg, pp. 375–388. https://doi.org/10.1007/978-3-642-33374-3_29.

Lee, S.K., Dang, T.A., 2019. Spatio-temporal variations in meteorological drought over the Mekong river delta of Vietnam in recent decades. Paddy Water Environ. 17, 35–44. https://doi.org/10.1007/s10333-018-0681-8.

Li, Z., Chen, Y., Yang, J., Wang, Y., 2014. Potential evapotranspiration and its attribution over the past 50 years in the arid region of Northwest China. Hydrol. Process. 28, 2751–2761. https://doi.org/10.1002/hyp.9643.

Li, B., Chen, F., Guo, H., 2015. Regional complexity in trends of potential evapotranspiration and its driving factors in the upper Mekong river basin. Quat. Int. 380–381, 83–94. https://doi.org/10.1016/j.quaint.2014.12.052.

Li, P., Furtado, K., Zhou, T., Chen, H., Li, J., Guo, Z., Xiao, C., 2020. The diurnal cycle of East Asian summer monsoon precipitation simulated by the met office unified model at convection-permitting scales. Clim. Dyn. 55, 131–151. https://doi.org/10.1007/s00382-018-4368-z.

Liu, W., Lim, W.H., Sun, F., Mitchell, D., Wang, H., Chen, D., Fischer, E., 2018. Global freshwater availability below normal conditions and population impact under 1.5°c and 2°c stabilization scenarios. Geophys. Res. Lett. 45, 9803–9813. https://doi.org/10.1029/2018GL078789.

Luo, X., Wu, W., He, D., Li, Y., Ji, X., 2019. Hydrological simulation using TRMM and CHIRPS precipitation estimates in the lower Lancang–Mekong River Basin. Chin. Geogr. Sci. 29, 13–25. https://doi.org/10.1007/s11769-019-1014-6.

Luong, V.V., 2021. Effects of ENSO and climate change on reference evapotranspiration in southern Vietnam. J. Meteorol. Res. 35, 868–881. https://doi.org/10.1007/s13351-021-1006-1.

Martens, B., Miralles, D.G., Lievens, H., van der Schalie, R., de Jeu, R.A.M., Fernández-Prieto, D., Beck, H.E., Dorigo, W.A., Verhoest, N.E.C., 2017. GLEAM v3: Satellite-based land evaporation and root-zone soil moisture. Geosci. Model Dev. 10, 1903–1925. https://doi.org/10.5194/gmd-10-1903-2017.

Marullo, S., Minnett, P.J., Santoleri, R., Tonani, M., 2016. The diurnal cycle of sea-surface temperature and estimation of the heat budget of the Mediterranean sea. J. Geophys. Res. Oceans 121 (11), 8351–8367. https://doi.org/10.1002/2016JC012192.

Mei, H., Liang, X.-Z., Zeng, M., Yang, Y., Sun, C., Li, X., 2024. Improving diurnal precipitation forecasts through coherent coupling of cumulus and planetary boundary layer parameterizations. J. Geophys. Res. Atmos. 129, e2023JD040295. https://doi.org/10.1029/2023JD040295.

Meroni, A.N., Ban, N., Schär, C., Scoccimarro, E., Fogli, P.G., 2021. Sensitivity of some african heavy rainfall events to microphysics and planetary boundary layer schemes: impacts on localised storms. Q. J. R. Meteorol. Soc. 147, 2448–2468. https://doi.org/10.1002/qj.4033.

Minh, H.V.T., Kumar, P., Ty, T.V., Duy, D.V., Han, T.G., Lavane, K., Avtar, R., 2022a. Understanding dry and wet conditions in the Vietnamese Mekong delta using multiple drought indices: a case study in Ca Mau province. Hydrology 9, 213. https://doi.org/10.3390/hydrology9120213.

Minh, H.V.T., Lavane, K., Ty, T.V., Downes, N.K., Hong, T.T.K., Kumar, P., 2022b. Evaluation of the impact of drought and saline water intrusion on rice yields in the Mekong Delta, Vietnam. Water 14, 3499. https://doi.org/10.3390/w14213499.

Mlawer, E.J., Taubman, S.J., Brown, P.D., Iacono, M.J., Clough, S.A., 1997. Radiative transfer for inhomogeneous atmospheres: RRTM, a validated correlated-k model for the long-wave. J. Geophys. Res. 102, 16663–16682. https://doi.org/10.1029/97JD00237.

Mohan, M., Bhati, S., 2011. Analysis of WRF model performance over subtropical region of Delhi, India. Adv. Meteorol. 2011, 621235. https://doi.org/10.1155/2011/621235.

Mondal, A., Le, M.-H., Lakshmi, V., 2022. Land use, climate, and water change in the Vietnamese Mekong delta (VMD) using earth observation and hydrological modeling. J. Hydrol. Region. Stud. 42, 101132. https://doi.org/10.1016/j.ejrh.2022.101132.

Mu, Q., Zhao, M., Running, S.W., 2011. Improvements to a MODIS global terrestrial evapotranspiration algorithm. Remote Sens. Environ. 115, 1781–1800. https://doi.org/10.1016/j.rse.2011.02.019.

Nakanishi, M., Niino, H., 2006. An improved Mellor–Yamada level-3 model: its numerical stability and application to a regional prediction of advection fog. Bound. Layer Meteorol. 119, 397–407. https://doi.org/10.1007/s10546-005-9030-8.

Nguyen, K.C., Katzfey, J.J., McGregor, J.L., 2014. Downscaling over Vietnam using the stretched-grid CCAM: verification of the mean and interannual variability of rainfall. Clim. Dyn. 43, 861–879. https://doi.org/10.1007/s00382-013-1976-5.

Niu, G.-Y., Yang, Z.-L., Mitchell, K.E., Chen, F., Ek, M.B., Barlage, M., Kumar, A., Manning, K., Niyogi, D., Rosero, E., Tewari, M., Xia, Y., 2011. The community Noah land surface model with multiparameterization options (Noah-MP): part 1. Model description and evaluation with local-scale measurements. J. Geophys. Res. Atmos. 116, D12109. https://doi.org/10.1029/2010JD015139.

Phan, V.T., Ngo-Duc, T., Ho, T.M.H., 2009. Seasonal and interannual variations of surface climate elements over Vietnam. Clim. Res. 40, 49–60. https://doi.org/10.3354/cr00824.

Phan, D.C., Trung, T.H., Truong, V.T., Sasagawa, T., Vu, T.P.T., Bui, D.T., Hayashi, M., Tadono, T., Nasahara, K.N., 2021. First comprehensive quantification of annual land use/cover from 1990 to 2020 across mainland Vietnam. Sci. Rep. 11, 9979. https://doi.org/10.1038/s41598-021-89034-5.

Pilatin, H., Yücel, I., Düzenli, E., Yılmaz, M.T., 2021. Sensitivity of WRF-derived hydrometeorological extremes to sea-surface temperatures in regions with complex topography and diverse climate. Atmos. Res. 264, 105816. https://doi.org/10.1016/j.atmosres.2021.105816.

Pleim, J.E., 2007. A combined local and nonlocal closure model for the atmospheric boundary layer. Part I: model description and testing. J. Appl. Meteorol. Climatol. 46, 1383–1395. https://doi.org/10.1175/JAM2539.1.

Prein, A.F., Rasmussen, C.L., Ikeda, K., Liu, P., Clark, M.P., Rasmussen, R.M., 2015. A review on regional convection-permitting climate modeling: demonstrations, prospects, and challenges. Rev. Geophys. 53, 323–361. https://doi.org/10.1002/2014RG000475.

Qian, Y., Yan, H., Berg, L.K., Hagos, S., Feng, Z., Yang, B., Huang, M., 2016. Assessing impacts of PBL and surface layer schemes in simulating the surface–atmosphere interactions and precipitation over the tropical ocean using observations from AMIE/DYNAMO. J. Clim. 29 (22), 8388–8404. https://doi.org/10.1175/JCLI-D-16-0040.1.

Que, L.-J., Que, W.-L., Feng, J.-M., 2016. Intercomparison of different physics schemes in the WRF model over the Asian summer monsoon region. Atmosph. Ocean. Sci. Lett. 9, 169–177. https://doi.org/10.1080/16742834.2016.1158618.

Raghavan, S.V., Ramasamy, V.V., Krishnan, S.S., 2015. Evaluation of WRF model rainfall simulations over southern Vietnam. Theor. Appl. Climatol. 121, 703–722. https://doi.org/10.1007/s00704-014-1246-5.

Reddy, P.S., Niyogi, D., Venkatesan, R., 2023. Sensitivity analysis of different parameterization schemes of the weather research and forecasting (WRF) model to simulate heavy rainfall events over the Mahi river basin, India. Agric. For. Meteorol. 353, 109885. https://doi.org/10.1016/j.agrformet.2023.109885.

Senatore, A., Mendicino, G., Knoche, H.R., Kunstmann, H., 2014. Sensitivity of modeled precipitation to sea surface temperature in regions with complex topography and coastlines: a case study for the Mediterranean. J. Hydrometeorol. 15, 2370–2396. https://doi.org/10.1175/JHM-D-13-089.1.

Seo, H., Subramanian, A.C., Miller, A.J., Cavanaugh, N.R., 2014. Coupled impacts of the diurnal cycle of sea surface temperature on the Madden–Julian oscillation. J. Clim. 27 (22), 8422–8443. https://doi.org/10.1175/JCLI-D-14-00141.1.

Shen, Y., Du, Y., 2023. Sensitivity of boundary layer parameterization schemes in a marine boundary layer jet and associated precipitation during a coastal warm-sector heavy rainfall event. Front. Earth Sci. 10, 1085136. https://doi.org/10.3389/feart.2022.1085136.

Shi, R., Chen, J., He, Y., Song, W., Li, D., Shu, Y., Wang, D., 2024. Evaluation of the performance of the latest WRF model (v4.5) in simulating surface elements and its sensitivity to the diurnal SST cycle in the South China Sea. Clim. Dyn. 62 (2), 1567–1584. https://doi.org/10.1007/s00382-023-06988-0.

Shin, H.H., Dudhia, J., 2016. Evaluation of PBL parameterizations in WRF at subkilometer grid spacings: Turbulence statistics in the dry convective boundary layer. Mon. Weather Rev. 144 (3), 1161–1177. https://doi.org/10.1175/MWR-D-15-0208.1.

Shuttleworth, W.J., 1993. Evaporation. In: Handbook of Hydrology. McGraw-Hill, New York, pp. 4.1–4.53.

Skamarock, W.C., Klemp, J.B., Dudhia, J., Gill, D.O., Liu, Z., Powers, J.G., Duda, M.G., Barker, D.M., Huang, X.-Y., 2019. A description of the Advanced Research WRF Model version 4.1. NCAR Technical Note NCAR/TN-556+STR. National Center for Atmospheric Research. https://doi.org/10.5065/1dfh-6p97.

Stan, F., Neculau, G., 2015. Estimation of reference evapotranspiration from pan evaporation data in Romania. Roman. J. Meteorol. 12, 1–2.

Subrahmanyam, K.V., Kumar, P., Nelli, N.R., Sampelli, A., Ramana, M.V., Rajeevan, M., Chauhan, P., 2025. Regional shift in the peak time of maximum Indian summer monsoon rainfall in recent decades. Geophys. Res. Lett. 52, e2024GL112697. https://doi.org/10.1029/2024GL112697.

Sun, C., Xiao, Z.-N., Nguyen, M.N., 2021. Projection on precipitation frequency of different intensities and precipitation amount in the Lancang–Mekong River Basin in the 21st century. Adv. Clim. Chang. Res. 12, 162–171. https://doi.org/10.1016/j.accre.2021.03.001.

Takahashi, H.G., Fujinami, H., Yasunari, T., Matsumoto, J., 2010. Diurnal rainfall pattern observed by tropical rainfall measuring mission precipitation radar (TRMM-PR) around the Indochina peninsula. J. Geophys. Res. Atmos. 115, D07109. https://doi.org/10.1029/2009JD012155.

Taraphdar, S., Pauluis, O.M., 2021. Impact of planetary boundary layer and cloud microphysics on the sensitivity of monsoon precipitation using a gray-zone regional model. Atmos. Res. 264, 105816. https://doi.org/10.1016/j.atmosres.2021.105816.

Taraphdar, S., Pauluis, O.M., Xue, L., Liu, C., Rasmussen, R., Ajayamohan, R.S., et al., 2021. WRF gray-zone simulations of precipitation over the Middle-East and the UAE: impacts of physical parameterizations and resolution. J. Geophys. Res. Atmos. 126, e2021JD034648. https://doi.org/10.1029/2021JD034648.

Taylor, K.E., 2001. Summarizing multiple aspects of model performance in a single diagram. J. Geophys. Res. 106, 7183–7192. https://doi.org/10.1029/2000JD900719.

Trinh-Tuan, L., Ngo-Duc, T., Phan-Van, T., Tran, H., Trinh, T., Pham-Quang, N., Nguyen, T., 2025. Future rainfall projections for the lower Mekong basin using CMIP6 dynamical downscaling. J. Water Clim. Chang. 16, 1863–1876. https://doi.org/10.2166/wcc.2025.793.

Truong, N.M., Bui, M.T., 2019. Structures and mechanisms of 20–60-day intraseasonal oscillation of the observed rainfall in Vietnam. J. Clim. 32 (16), 5191–5212. https://doi.org/10.1175/JCLI-D-18-0239.1.

Truong, N.M., Tuan, B.M., 2018. Large-scale patterns and possible mechanisms of 10–20-day intraseasonal oscillation of the observed rainfall in Vietnam. Int. J. Climatol. 38 (10), 3801–3821. https://doi.org/10.1002/joc.5534.

Vörösmarty, C.J., Green, P., Salisbury, J., Lammers, R.B., 2000. Global water resources: vulnerability from climate change and population growth. Science 289, 284–288. https://doi.org/10.1126/science.289.5477.284.

Wang, Z., Duan, A., Wu, G., 2014. Impacts of boundary layer parameterization schemes and air–sea coupling on WRF simulation of the East Asian summer monsoon. Sci. China Earth Sci. 57, 1480–1493. https://doi.org/10.1007/s11430-013-4801-4.

Wei, L., Rucong, Y., Hailong, H., Yongqiang, Y., 2001. Impacts of the diurnal cycle of SST on the intraseasonal variation of surface heat flux over the western pacific warm pool. Adv. Atmos. Sci. 18, 793–806. https://doi.org/10.1007/BF03403503.

Wilder, M., Phuong, N.T., 2002. The status of aquaculture in the Mekong delta region of Vietnam: Sustainable production and combined farming systems. Fish. Sci. 68, 847–850. https://doi.org/10.2331/fishsci.68.sup1_847.

Xie, B., Fung, J.C.H., Chan, A., Lau, A., 2012. Evaluation of nonlocal and local planetary boundary layer schemes in the WRF model. J. Geophys. Res. Atmos. 117, D12103. https://doi.org/10.1029/2011JD017080.

Xu, Y.-P., Gao, H.-J., Chang, H.T., Wang, F., Liu, C.-L., 2014. Future potential evapotranspiration changes and contribution of climatic and non-climatic drivers in a changing environment. J. Geophys. Res. Atmos. 119, 2174–2196. https://doi.org/10.1002/2013JD021245.

Xu, L., Pyles, R.D., Paw U, K.T., Snyder, R., Monier, E., Falk, M., Chen, S.-H., 2017. Impact of canopy representations on regional modeling of evapotranspiration using the WRF–ACASA coupled model. Agric. For. Meteorol. 247, 79–92. https://doi.org/10.1016/j.agrformet.2017.07.003.

Yang, Z.-L., Niu, G.-Y., Mitchell, K.E., Chen, F., Ek, M.B., Barlage, M., Longuevergne, L., Manning, K., Niyogi, D., Tewari, M., Xia, Y., 2011. The community Noah land surface model with multiparameterization options (Noah-MP): part 2. Evaluation over global river basins. J. Geophys. Res. Atmos. 116, D12110. https://doi.org/10.1029/2010JD015140.

Yang, B., Zhou, Y., Zhang, Y., Huang, A., Qian, Y., Zhang, L., 2018. Simulated precipitation diurnal cycles over East Asia using different CAPE-based convective closure schemes in the WRF model. Clim. Dyn. 50, 1639–1658. https://doi.org/10.1007/s00382-017-3712-z.

Yin, Y., Wu, S., Chen, G., Dai, E., et al., 2010. Attribution analyses of potential evapotranspiration changes in China since the 1960s. Theor. Appl. Climatol. 101, 19–28. https://doi.org/10.1007/s00704-009-0197-7.

Zeng, X., Beljaars, A., 2005. A prognostic scheme of sea surface skin temperature for modeling and data assimilation. Geophys. Res. Lett. 32, L14605. https://doi.org/10.1029/2005GL023030.

Zhang, Y., Chen, H., 2016. Comparing CAM5 and super-parameterized CAM5 simulations of summer precipitation characteristics over continental East Asia: mean state, frequency–intensity relationship, diurnal cycle, and influencing factors. J. Clim. 29, 1067–1089. https://doi.org/10.1175/JCLI-D-15-0342.1.

Zhang, H., Beggs, H., Merchant, C.J., Wang, X.H., Majewski, L., Kiss, A.E., Rodríguez, A., 2016. Investigating sea surface temperature diurnal variation over the tropical warm pool using MTSAT-1R data. Remote Sens. Environ. 183, 1–12. https://doi.org/10.1016/j.rse.2016.05.002.

Zhang, H., Beggs, H., Merchant, C.J., Wang, X.H., Majewski, L., Kiss, A.E., Brunke, M., 2018. Comparison of SST diurnal variation models over the tropical warm pool region. J. Geophys. Res. Oceans 123, 3467–3488. https://doi.org/10.1029/2017JC013517.

Zhao, F., Ma, S., Wu, Y., 2021. Changes in dry-season water availability and attributions in the Yellow River basin, China. Front. Environ. Sci. 9, 762137. https://doi.org/10.3389/fenvs.2021.762137.

Zhong, Z., He, Y., Ma, J., Xu, H., 2007. Numerical experiments on the spin-up time for seasonal-scale regional climate modeling. Acta. Meteor. Sin. 21, 409–419.

Zhou, P., Shao, M., Ma, M., Ou, T., Tang, J., 2022. WRF gray-zone dynamical downscaling over the Tibetan plateau during 1999–2019: Model performance and added value. Clim. Dyn. 61, 1371–1390. https://doi.org/10.1007/s00382-022-06631-4.

Zhu, L., Meng, Z., Zhang, F., Markowski, P.M., 2017. The influence of sea-and land-breeze circulations on the diurnal variability in precipitation over a tropical island. Atmos. Chem. Phys. 17 (21), 13213–13232. https://doi.org/10.5194/acp-17-13213-2017.